APPLICATION OF AN EXTENDED ELIASHBERG THEORY TO HIGH-T_c CUPRATES

E. Schachinger[1], J. P. Carbotte[2]
[1] *Institut für Theoretische Physik, Technische Universität Graz*
A–8010 Graz, Austria
[2] *Department of Physics & Astronomy, McMaster University*
Hamilton, Ontario, Canada L8S 4M1

(Received June 15, 2002)

In recent years a unified phenomenological picture for the hole doped high-T_c cuprates has emerged for a spin and charge spectroscopy. Spectral anomalies have been interpreted as evidence of charge carrier coupling to a collective spin excitation present in the optical conductivity, in ARPES (angular resolved photoemission), and in tunneling data. These anomalies can be used to derive an approximate picture of a charge carrier — exchange boson interaction spectral density $I^2\chi(\omega)$ which is then to be used within an extended Eliashberg formalism to analyze normal and superconducting properties of optimally doped and overdoped cuprates. This paper reviews recent developments and demonstrates the sometimes astonishing agreement between experiment and theoretical prediction.

Key words: Eliashberg theory, high-T_c superconductivity, optical conductivity, pairing models.

PACS number(s): 74.20.Mn, 74.25.Gz, 74.72.–h

I. INTRODUCTION

The standard Eliashberg equations [1,2] were derived for superconductors with an energy gap of s-wave symmetry and the electron-phonon interaction as the pairing interaction. This type of interaction allows the application of Migdal's theorem which states that vertex corrections in the electron-phonon interaction can be neglected to order $\omega_{\rm D}/\varepsilon_{\rm F}$, with $\omega_{\rm D}$ the Debye energy and $\varepsilon_{\rm F}$ the Fermi energy. On the other hand, it is now widely accepted that the high T_c cuprates have an energy gap of $d_{x^2-y^2}$ symmetry [3–8] and there is still no consensus as to the microscopic mechanism leading to Cooper pairs in these materials.

In Eliashberg theory a given superconductor is characterized by the Eliashberg function $\alpha^2F(\omega)$ which describes the exchange of a phonon by two electrons at the Fermi surface and by the Coulomb potential $\mu^\star$. These are the kernels in the two non-linear coupled Eliashberg equations. One equation, which is referred to as the renormalization channel, describes the effect of the electron–phonon interaction on normal-state properties modified further by the onset of superconductivity. The second equation, referred to as the pairing channel, deals with the energy gap directly and is identically zero in the normal-state. When reliable tunneling data is available for the quasiparticle density-of-states $N_{qp}(\omega)$, for instance, the procedure can be inverted [9,10] to get from $N_{qp}(\omega)$ the kernels $\alpha^2F(\omega)$ and $\mu^\star$. In principle, it should also be possible to get the same information from infrared data [11–13] although in conventional systems this has not been widely done while tunneling has. Once the kernels $\alpha^2F(\omega)$ and $\mu^\star$ are known, the finite temperature Eliashberg equations can be solved numerically to obtain superconducting properties.

In principle, the Eliashberg equations can easily be generalized to include d-wave symmetry of the energy gap by an appropriate extension (to include a dependence on orientation of the electron momenta) of the charge carrier — exchange boson interaction spectral density ($\alpha^2F(\omega)$ in case of the electron–phonon interaction) which contains all the relevant information about the coupling of the charge carriers to the exchange bosons. As the microscopic mechanism leading to superconductivity is not yet known, information on the charge carrier — exchange boson interaction spectral density (denoted $I^2\chi(\omega)$ throughout this paper) is to be obtained by a fit to appropriate data sets using phenomenological models. Such a procedure can yield a first approximation to a complete description even in cases when an equivalent to Migdal's theorem is not applicable and vertex corrections are not entirely negligible.

Unfortunately, the well established inversion techniques which allowed one to determine $\alpha^2F(\omega)$ from tunneling experiments [10] have, so far, not been extended to the cuprates and, therefore, phenomenological models had to be developed for $I^2\chi(\omega)$. One such phenomenological model has been introduced by Schachinger *et al.* [14–16] and was reviewed by Schachinger and Schürrer [17]. This model is a purely electronic model and describes the feedback effect the superconducting state has on $I^2\chi(\omega)$. The authors used, for definiteness, the spin fluctuation model introduced by Pines and coworkers [18,19] in their Nearly Antiferromagnetic Fermi Liquid (NAFFL) model. The feedback effect caused by superconductivity is described by introducing a low energy gap in $I^2\chi(\omega)$ (low frequency cutoff) which opens up as the temperature is lowered through the critical temperature T_c. This gap shows the same temperature dependence and size as the superconducting energy gap. Within this model it was possible to describe consistently the temperature dependence of the microwave conductivity with its pronounced peak around 40 K observed in optimally doped $YBa_2Cu_3O_{6.95}$ (YBCO) [20,21], the similar peak observed in the electronic thermal conductivity [22], and the temperature dependence of the penetration depth in nominally pure YBCO samples and in YBCO samples with Zn or Ni impurities [14]. Nevertheless, similar results would have been achieved using the Marginal Fermi Liquid (MFL) model [23] assuming a d-wave gap together with a low frequency cutoff to describe the charge carrier — exchange boson interaction spectral density.

A remarkable step forward in the development of phenomenological models was provided by the work of Marsiglio *et al.* [24] who were able to show analytically that there exists a simple, approximate formula which relates $\alpha^2F(\omega)$ to the normal state optical conductivity $\sigma(\omega)$ via the second derivative of the real part of $\omega\sigma^{-1}(\omega)$. This established the basis for a spectroscopy which allows the measurement of the spectral density $\alpha^2F(\omega)$ directly from optical data. This result was then extended to the superconducting state of d-wave superconductors by Carbotte *et al.* [25] who explore the relationship between spectral density and $W(\omega)$ at low temperatures in the superconducting state. They conclude that the relationship is not at all as direct, but, even though more complicated, it remains simple enough to be very useful although more approximate. (A similar procedure was also suggested by Munzar *et al.* [26].)

It will be the purpose of this paper to review the application of this technique to various cuprates in some detail. Thus, the paper establishes in section two the formalism, section three discusses its application to optimally doped YBCO. Other cuprates are also investigated within the same context, and finally, in section four a summary is presented.

II. FORMALISM

A. The Normal State Optical Conductivity

The optical conductivity is related to the current-current correlation function. The paramagnetic part of the response function on the imaginary frequency axis is given by [27–31]

$$\Pi(i\nu_n) = \frac{1}{N\beta}\sum_{\mathbf{k},m}(ev_x)^2\mathrm{tr}\left\{\hat{G}(\mathbf{k},i\omega_m)\hat{G}(\mathbf{k},i\omega_m+i\nu_n)\right\}, \tag{1}$$

where $\hat{G}(\mathbf{k},i\omega_m)$ is a matrix Green's function in the Nambu formalism [32], $i\omega_m = i\pi T(2m+1), m = 0,\pm1,\pm2,\ldots$ is the fermion and $i\nu_n = 2in\pi T, n = 0,\pm1,\pm2,\ldots$ is the boson Matsubara frequency; T is the temperature and v_x the component of the electron velocity in x-direction. The factors preceding the summations include the total number of atoms in the crystal, N, and the inverse temperature, $\beta \equiv 1/k_\mathrm{B}T$.

The optical conductivity is related to the response function through

$$\sigma(\omega) = \frac{i}{\omega}\Pi(\omega+i0^+). \tag{2}$$

After analytical continuation to the real frequency axis and using the usual procedure

$$\frac{1}{N}\sum_{\mathbf{k}} \quad \longrightarrow \int d\varepsilon\, N(\varepsilon),$$

we arrive at a general expression for the optical conductivity $\sigma'(\omega)$:

$$\begin{aligned}\sigma'(\omega) = \frac{1}{i\omega}&\left(\int_{-\infty}^{0} d\nu\,\tanh\left(\frac{\nu+\omega}{2T}\right)S^{-1}(T,\omega,\nu)\right)\\ &+\left(\int_{0}^{\infty} d\nu\left[\tanh\left(\frac{\nu+\omega}{2T}\right)\right.\right.\\ &\left.\left.-\tanh\left(\frac{\nu}{2T}\right)\right]S^{-1}(T,\omega,\nu)\right),\end{aligned} \tag{3}$$

which has been given by Lee *et al.* [28] (with the factor ne^2/m suppressed). Here, $N(\varepsilon) \equiv N(\varepsilon_\mathrm{F}) \equiv N(0)$, $N(0)e^2v_\mathrm{F}^2 = \Omega_p^2/4\pi \equiv ne^2/m$; Ω_p is the plasma frequency, e the charge on the electron, m its mass, and n the electron density per unit volume. In Eq. (3)

$$S(T,\omega,\nu) = \omega + \Sigma^\star(T,\nu+\omega) - \Sigma(T,\nu) - i\pi t^+ \tag{4}$$

with the self energy $\Sigma(T,\omega)$ related to the electron-phonon spectral density by

$$\begin{aligned}\Sigma(T,\omega) = -\int dz\,\alpha^2F(z)&\left[\psi\left(\frac{1}{2}+i\frac{\omega+z}{2\pi T}\right)\right.\\ &\left.-\psi\left(\frac{1}{2}+i\frac{\omega-z}{2\pi T}\right)\right],\end{aligned} \tag{5}$$

where ψ is the digamma function. In Eq. (4) $\pi t^+ \equiv 1/(2\tau_\mathrm{imp})$ gives the impurity contribution to the electronic scattering. (τ_imp is the impurity scattering time.)

At zero temperature these expressions for the conductivity reduce to a simple form [24,33]:

$$\sigma(\omega) = \frac{\Omega_p^2}{4\pi}\frac{i}{\omega}\int_0^\omega d\nu\,\frac{1}{\omega-\Sigma(\nu)-\Sigma(\omega-\nu)}, \tag{6}$$

and the self energy

$$\Sigma(\omega) = \int_0^\infty d\Omega\, \alpha^2 F(\Omega) \ln\left|\frac{\Omega-\omega}{\Omega+\omega}\right| - i\pi \int_0^{|\omega|} d\Omega\, \alpha^2 F(\Omega)$$

for the electron–phonon interaction. In this form Marsiglio *et al.* [24] were able to show analytically that a remarkably simple formula could be used to establish an approximate but very useful relationship between $\sigma(\omega)$ and $\alpha^2F(\omega)$. The observation was also backed up by detailed numerical work. We begin by defining an optical scattering rate $\tau_{\rm op}^{-1}(\omega)$ as [24,25]

$$\frac{1}{\tau_{\rm op}(\omega)} = \frac{\Omega_p^2}{4\pi}\Re\mathrm{e}\frac{1}{\sigma(\omega)} \equiv \Re\mathrm{e}\frac{1}{\sigma'(\omega)}, \qquad (7)$$

which is routinely obtained in optical experiments. We then define an auxiliary function [24,25]

$$W(\omega) \equiv \frac{1}{2\pi}\frac{d^2}{d\omega^2}\left\{\frac{\omega}{\tau_{\rm op}(\omega)}\right\}. \qquad (8)$$

Marsiglio *et al.* [24] have shown that in certain circumstances

$$\alpha^2F(\omega) \simeq W(\omega), \qquad (9)$$

which serves as a basis for a spectroscopy which allows the measurement of the spectral density $\alpha^2F(\omega)$ directly from optical data. In Fig. 1 we show theoretical results for $W(\omega)$ at two temperatures based on the case of Pb. The solid curve is the Pb $\alpha^2F(\omega)$ obtained from tunneling data. The other two curves were obtained by calculating $\sigma(\omega)$ from Eq. (3) and computing $W(\omega)$ defined by Eq. (8). Such calculations were performed at two temperatures, namely $T = 1\,$K (dotted) and $T = 14\,$K (dash-dotted). Within the energy range corresponding to the range of $\alpha^2F(\omega)$ the dotted curve for $W(\omega)$ is remarkably close to the solid curve for $\alpha^2F(\omega)$ and therefore $W(\omega)$ gives an accurate measurement of the absolute value as well as the frequency dependence of the spectral density. As the temperature is increased this is no longer the case although some rough correspondence remains which provides a qualitative similarity between the two quantities which could still be exploited to get a rough first measure of the spectral density in cases where low temperature data are not available. We point out that even at $T = 1\,$K there are negative tails in $W(\omega)$ above the maximum phonon cutoff which are not in $\alpha^2F(\omega)$. This is expected since $W(\omega)$ and $\alpha^2F(\omega)$ are not the same quantities. In fact, it is indeed remarkable that they should correspond so closely below the phonon cutoff energy. This close correspondence can be exploited to get a good first measure of the spectral density $\alpha^2F(\omega)$ from infrared data. In principle, one should use the first iteration for $\alpha^2F(\omega)$ obtained from the second derivative of the conductivity defining $W(\omega)$ [Eq. (8)], to calculate from it $\sigma(\omega)$ based on Eqs. (3) to (5) and keep iterating until an exact correspondence between calculated and measured $\sigma(\omega)$ results has been achieved. In any of the applications so far this has not been attempted because of the many uncertainties that remain.

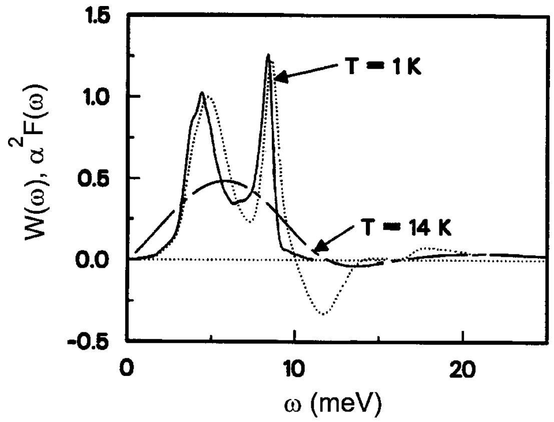

Fig. 1. The solid curve is $\alpha^2F(\omega)$ *vs.* ω for Pb. The other curves are the function $W(\omega)$ according to Eq. (8) obtained from the normal-state conductivity optical scattering rate $\tau_{\rm op}^{-1}(\omega)$ at various temperatures. See Marsiglio *et al.* [24].

B. The Superconducting State

In as much as BCS theory applies, any effective interaction between two electrons at the Fermi surface, which is attractive, will lead to superconductivity. This can arise from the electron–phonon interaction through the polarization of the system of ions. In this case we can describe the polarization process as due to the exchange of a phonon between a pair of charge carriers. An obvious extension is to ask: could we exchange some other excitation? In the Nearly Antiferromagnetic Fermi Liquid (NAFFL) model of Pines and coworkers [18,19] it is envisaged that spin fluctuations replace the phonons. The basic formalism for dealing with this new situation are the Eliashberg equations but now the $\mathbf{k}, \mathbf{k}'$ anisotropy in momentum of the kernel $\alpha^2_{\mathbf{kk}'}F(\omega)$ needs to be taken into account so that the resulting superconducting state exhibits d-wave symmetry to accord with the experimental observation. In the renormalization channel we take for simplicity only the isotropic contribution from the electron–spin fluctuation exchange written as $I^2\chi(\omega)$ where I^2 is to denote a spin–charge exchange coupling constant and $\chi(\omega)$ is the spin susceptibility. To get a d-wave gap we use a separable interaction of the form $\cos(2\theta)gI^2\chi(\omega)\cos(2\theta')$ with θ and θ' the direction of the initial ($\mathbf{k}$) and final ($\mathbf{k}'$) momentum which, for simplicity, we pin on the Fermi surface although in the NAFFL the entire Brillouin zone is averaged over i.e.: is not pinned on the Fermi surface. While, for simplicity, we have assumed the same form $I^2\chi(\omega)$ to hold in the pairing as in the renormalization channel we have introduced a numerical factor g to account for the fact that the projection of the general spectral density will in general be different in the two channels. The repulsive effective Coulomb interaction $\mu^\star_{\mathbf{k},\mathbf{k}'}$ is isotropic in an isotropic s-wave formalism. The same holds for the 'Hubbard' U which is also assumed to be large and isotropic. Thus, the effective Coulomb potential is not expected to have a numerically large d-wave symmetric part and therefore does not contribute to the pairing channel in a generalized d-wave formulation of the Eliashberg equations.

Within these simplifying assumptions the Eliashberg equations need first to be written on the imaginary Matsubara frequency axis. They take on the following form [34]:

$$\tilde\Delta(i\omega_n;\theta) = g\pi T\sum_m \cos(2\theta)\lambda(m-n) \times\left\langle\frac{\cos(2\theta')\tilde\Delta(i\omega_m;\theta')}{\sqrt{\tilde\omega^2(i\omega_m)+\tilde\Delta^2(i\omega_m;\theta')}}\right\rangle', \tag{10a}$$

for the renormalized pairing potential $\tilde\Delta(i\omega_n;\theta)$, and

$$\tilde\omega(i\omega_n) = \omega_n + \pi T\sum_m \lambda(m-n) \times\left\langle\frac{\tilde\omega(i\omega_m)}{\sqrt{\tilde\omega^2(i\omega_m)+\tilde\Delta^2(i\omega_m;\theta')}}\right\rangle', \tag{10b}$$

for the renormalized frequencies $\tilde\omega(i\omega_n)$. Here, $\langle\cdots\rangle$ denotes the angular average over θ. The quantity $\lambda(m-n)$ has the usual form

$$\lambda(m-n) = 2\int_0^\infty d\Omega\,\frac{\Omega I^2\chi(\omega)}{\Omega^2+(\omega_m-\omega_n)^2}. \tag{10c}$$

As written, Eqs. (10) do not depend on impurity scattering. To include this possibility, we need to add into the right hand side of Eq. (10b) a term of the form

$$\pi\Gamma^+\frac{\Omega(i\omega_n)}{c^2+\Omega^2(i\omega_n)+D^2(i\omega_n)} \tag{11}$$

where Γ^+ is proportional to the impurity concentration and c is related to the electron phase shift for scattering off the impurity. For unitary scattering, c is equal to zero while $c\to\infty$ gives the Born approximation, i. e.: the weak scattering limit. In this case the entire impurity term reduces to the form $\pi t^+\Omega(i\omega_n)$ with c absorbed into t^+. To complete the specification of Eq. (11), we have

$$D(i\omega_n) = \left\langle\frac{\tilde\Delta(i\omega_n;\theta)}{\sqrt{\tilde\omega^2(i\omega_m)+\tilde\Delta^2(i\omega_m;\theta)}}\right\rangle, \tag{12a}$$

and

$$\Omega(i\omega_n) = \left\langle\frac{\tilde\omega(i\omega_n)}{\sqrt{\tilde\omega^2(i\omega_m)+\tilde\Delta^2(i\omega_m;\theta)}}\right\rangle. \tag{12b}$$

While certain quantities, such as the penetration depth, can be obtained quite directly from the numerical solution on the imaginary frequency axis, i. e.: from $\tilde\Delta(i\omega_n;\theta)$ and $\tilde\omega(i\omega_n)$, real frequency axis solutions are needed to calculate the optical conductivity. These equations for $\tilde\Delta(\nu+i\delta;\theta)$ and $\tilde\omega(\nu+i\delta)$ with δ infinitesimal are more complicated and can be written in the form [14–16]:

$$\tilde\Delta(\nu+i\delta;\theta) = \pi Tg\sum_{m=0}^\infty \cos(2\theta)\left[\lambda(\nu-i\omega_m)+\lambda(\nu+i\omega_m)\right]\left\langle\frac{\tilde\Delta(i\omega_m;\theta')\cos(2\theta')}{\sqrt{\tilde\omega^2(i\omega_m)+\tilde\Delta^2(i\omega_m;\theta')}}\right\rangle' + i\pi g\int_{-\infty}^\infty dz\,\cos(2\theta)I^2\chi(z)\left[n(z)+f(z-\nu)\right]\left\langle\frac{\tilde\Delta(\nu-z+i\delta;\theta')\cos(2\theta')}{\sqrt{\tilde\omega^2(\nu-z+i\delta)-\tilde\Delta^2(\nu-z+i\delta;\theta')}}\right\rangle', \tag{13a}$$

for the pairing channel and

$$\tilde\omega(\nu+i\delta) = \nu + i\pi T\sum_{m=0}^\infty\left[\lambda(\nu-i\omega_m)-\lambda(\nu+i\omega_m)\right]\left\langle\frac{\tilde\omega(i\omega_m)}{\sqrt{\tilde\omega^2(i\omega_m)+\tilde\Delta^2(i\omega_m;\theta')}}\right\rangle' \tag{13b}$$

$$+ i\pi \int_{-\infty}^{\infty} dz\, I^2\chi(z)\,[n(z)+f(z-\nu)] \left\langle \frac{\tilde{\omega}(\nu-z+i\delta)}{\sqrt{\tilde{\omega}^2(\nu-z+i\delta)-\tilde{\Delta}^2(\nu-z+i\delta;\theta')}} \right\rangle' + i\pi\Gamma^+ \frac{\Omega(\nu)}{c^2+D^2(\nu)+\Omega^2(\nu)}.$$

for the renormalization channel. Thermal factors appear in these equations through the Bose and Fermi distribution $n(z)$ and $f(z)$, respectively. Furthermore, the abbreviations:

$$\lambda(\nu) = \int_{-\infty}^{\infty} d\Omega\, \frac{I^2\chi(\Omega)}{\nu-\Omega+i0^+}, \tag{14a}$$

$$D(\nu) = \left\langle \frac{\tilde{\Delta}(\nu+i\delta;\theta)}{\sqrt{\tilde{\omega}^2(\nu+i\delta)-\tilde{\Delta}^2(\nu+i\delta;\theta)}} \right\rangle, \tag{14b}$$

$$\Omega(\nu) = \left\langle \frac{\tilde{\omega}(\nu+i\delta)}{\sqrt{\tilde{\omega}^2(\nu+i\delta)-\tilde{\Delta}^2(\nu+i\delta;\theta)}} \right\rangle. \tag{14c}$$

have been used. Eqs. (13) are a set of nonlinear coupled equations for the renormalized pairing potential $\tilde{\Delta}(\nu+i\delta;\theta)$ and the renormalized frequencies $\tilde{\omega}(\nu+i\delta)$ with the superconducting gap given by

$$\Delta(\nu+i\delta;\theta) = \nu\, \frac{\tilde{\Delta}(\nu+i\delta;\theta)}{\tilde{\omega}(\nu+i\delta)}, \tag{15}$$

or, if the renormalization function $Z(\nu)$ is introduced in the usual way as $\tilde{\omega}(\nu+i\delta) = \nu Z(\nu)$, one finds for the superconducting gap

$$\Delta(\nu+i\delta;\theta) = \frac{\tilde{\Delta}(\nu+i\delta;\theta)}{Z(\nu)}. \tag{16}$$

These equations are a minimum set and go beyond a BCS approach and include the inelastic scattering known to be strong in the cuprate superconductors.

From solutions of the generalized Eliashberg equations we can construct the Green's function in Eq. (1) analytically continued to the real frequency axis Ω. In this formulation the expression for the in-plane conductivity $\sigma_{ab}(T,\Omega)$ involves further averaging over angles which needs to be done numerically. We find the following result after further manipulations and rearrangements:

$$\begin{aligned}
\sigma_{ab}(\Omega) = \frac{i}{\Omega}\frac{e^2N(0)v_F^2}{2} \Bigg\langle & \int_0^{\infty} \mathrm{d}\nu \tanh\left(\frac{\nu}{2T}\right) \frac{1-N(\nu;\theta)N(\nu+\Omega;\theta)-P(\nu;\theta)P(\nu+\Omega;\theta)}{E(\nu;\theta)+E(\nu+\Omega;\theta)} \\
&+ \int_0^{\infty} \mathrm{d}\nu \tanh\left(\frac{\nu+\Omega}{2T}\right) \frac{1-N^\star(\nu;\theta)N^\star(\nu+\Omega;\theta)-P^\star(\nu;\theta)P^\star(\nu+\Omega;\theta)}{E^\star(\nu;\theta)+E^\star(\nu+\Omega;\theta)} \\
&+ \int_0^{\infty} \mathrm{d}\nu \left[\tanh\left(\frac{\nu+\Omega}{2T}\right)-\tanh\left(\frac{\nu}{2T}\right)\right] \frac{1+N^\star(\nu;\theta)N(\nu+\Omega;\theta)+P^\star(\nu;\theta)P(\nu+\Omega;\theta)}{E(\nu+\Omega;\theta)-E^\star(\nu;\theta)} \\
&+ \int_{-\Omega}^{0} \mathrm{d}\nu \tanh\left(\frac{\nu+\Omega}{2T}\right) \Bigg\{ \frac{1-N^\star(\nu;\theta)N^\star(\nu+\Omega;\theta)-P^\star(\nu;\theta)P^\star(\nu+\Omega;\theta)}{E^\star(\nu;\theta)+E^\star(\nu+\Omega;\theta)} \\
&+ \frac{1+N^\star(\nu;\theta)N(\nu+\Omega;\theta)+P^\star(\nu;\theta)P(\nu+\Omega;\theta)}{E(\nu+\Omega;\theta)-E^\star(\nu;\theta)} \Bigg\} \Bigg\rangle,
\end{aligned} \tag{17a}$$

with

$$E(\omega;\theta) = \sqrt{\tilde{\omega}_{\mathbf{k}}^2(\omega)-\tilde{\Delta}_{\mathbf{k}}^2(\omega)}, \tag{17b}$$

and

$$N(\omega;\theta)=\frac{\tilde{\omega}_{\mathbf{k}}(\omega)}{E(\omega;\theta)},\qquad P(\omega;\theta)=\frac{\tilde{\Delta}_{\mathbf{k}}(\omega)}{E(\omega;\theta)}. \tag{17c}$$

In the above, the star refers to the complex conjugate. This set of equations is valid for the real and imaginary part of the conductivity as a function of frequency Ω. It contains only the paramagnetic contribution to the conductivity but this is fine since we have found that the diamagnetic contribution is small in the case considered here.

The out-of-plane conductivity $\sigma_c(T,\Omega)$ at temperature T and frequency Ω is related to the current–current correlation function $\Pi_c(T,i\nu_n)$ at the boson Matsubara frequency $i\nu_n$ analytically continued to real frequency Ω, and to the c-axis kinetic energy $\langle H_c\rangle$ [35,36] via

$$\sigma_c(T,\Omega)=\frac{1}{\Omega}\left[\Pi_c(T,i\nu_n\to\Omega+i0^+)-e^2d^2\langle H_c\rangle\right], \tag{18}$$

with d the distance between planes in c-direction. In terms of the in-plane thermodynamic Green's function $\hat{G}(\mathbf{k},i\omega_n)$ and for coherent hopping $t_\perp(\mathbf{k})$ perpendicular to the CuO_2 planes

$$\Pi_c(T,i\nu_n)=2(ed)^2T\sum_{\omega_m}\sum_{\mathbf{k}}t_\perp^2(\mathbf{k})$$
$$\times\mathrm{tr}\left\{\hat{\tau}_0\hat{G}(\mathbf{k},i\omega_m)\hat{\tau}_0\hat{G}(\mathbf{k},i\omega_m+i\nu_n)\right\} \tag{19a}$$

and

$$\langle H_c\rangle=2T\sum_{\omega_m}\sum_{\mathbf{k}}t_\perp^2(\mathbf{k})\,\mathrm{tr}\left\{\hat{\tau}_3\hat{G}(\mathbf{k},i\omega_m)\hat{\tau}_3\hat{G}(\mathbf{k},i\omega_m)\right\}. \tag{19b}$$

In Eqs. (19) the 2×2 Nambu Green's function $\hat{G}(\mathbf{k},i\omega_m)$ describes the in-plane dynamics of the charge carriers with momentum $\mathbf{k}$ in the two dimensional CuO_2 plane Brillouin zone and is given by

$$\hat{G}(\mathbf{k},i\omega_n)=\frac{i\tilde{\omega}(i\omega_n)\hat{\tau}_0+\zeta_{\mathbf{k}}\hat{\tau}_3+\tilde{\Delta}_{\mathbf{k}}(i\omega_n)\hat{\tau}_1}{-\tilde{\omega}^2(i\omega_n)-\zeta_{\mathbf{k}}^2-\tilde{\Delta}_{\mathbf{k}}^2(i\omega_n)}, \tag{20}$$

where the $\hat{\tau}$'s are Pauli 2×2 matrices, $\zeta_{\mathbf{k}}$ is the band energy of the charge carriers as a function of their momentum $\mathbf{k}$, $\tilde{\Delta}_{\mathbf{k}}(i\omega_n)$ is the renormalized pairing potential and $i\tilde{\omega}(i\omega_n)$ the renormalized Matsubara frequency. In our model these quantities are determined as solutions of Eliashberg equations (10).

In Eqs. (19) the out-of-plane matrix element $t_\perp(\mathbf{k})$ can depend on the in-plane momentum $\mathbf{k}$. Models have been summarized recently by Sandeman and Schofield [37] who refer to previous literature [38–40]. A possible choice is $t_\perp(\mathbf{k})=t_\perp$, a constant. But, consideration of the chemistry of the CuO_2 plane and of the overlap of one plane with the next, suggests a form $t_\perp(\mathbf{k})=\cos^2(2\theta)$ where θ is the angle of $\mathbf{k}$ in the two dimensional CuO_2 Brillouin zone for the plane motion. This matrix element eliminates entirely contributions from nodal quasiparticles to the c-axis motion.

For incoherent impurity induced c-axis charge transfer Eqs. (19) are to be modified. After an impurity configuration average one obtains

$$\Pi_c(T,i\nu_n)=2(ed)^2T\sum_m\sum_{\mathbf{k},\mathbf{k}'}\overline{V^2_{\mathbf{k},\mathbf{k}'}}$$
$$\times\ \mathrm{tr}\left\{\hat{\tau}_0\hat{G}(\mathbf{k},i\omega_m)\hat{\tau}_0\hat{G}(\mathbf{k}',i\omega_m+i\nu_n)\right\} \tag{21a}$$
$$\langle H_c\rangle=2T\sum_m\sum_{\mathbf{k},\mathbf{k}'}\overline{V^2_{\mathbf{k},\mathbf{k}'}}$$
$$\times\ \mathrm{tr}\left\{\hat{\tau}_3\hat{G}(\mathbf{k},i\omega_m)\hat{\tau}_3\hat{G}(\mathbf{k}',i\omega_m)\right\}, \tag{21b}$$

with $\overline{V^2_{\mathbf{k},\mathbf{k}'}}$ the average of the square of the impurity potential. If the impurity potential was taken to conserve momentum, which it does not, we would recover Eqs. (19). Various models could be taken for $\overline{V^2_{\mathbf{k},\mathbf{k}'}}$. Here we use a form introduced by Kim [35] and Hirschfeld *et al.* [41]

$$\overline{V^2_{\mathbf{k},\mathbf{k}'}}=|V_0|^2+|V_1|^2\cos(2\theta)\cos(2\theta'), \tag{22}$$

with θ and θ' the directions of $\mathbf{k}$ and $\mathbf{k}'$ respectively.

After analytic continuation to the real Ω-axis the real part of the incoherent conductivity along the c-axis is given by (normalized to its normal state value σ_{1cn}) [41]:

$$\frac{\sigma_{1c}(\Omega)}{\sigma_{1cn}}=\frac{1}{\nu}\int d\omega\ [f(\omega)-f(\omega+\Omega)] \tag{23}$$
$$\times\left[N(\omega+\Omega)N(\omega)+\left|\frac{V_1}{V_0}\right|P(\omega+\Omega)P(\omega)\right].$$

III. APPLICATION TO HIGH-T_C CUPRATES

A. The Compound $YBa_2Cu_3O_{6+\delta}$

1. The Normal State Infrared Conductivity

We begin with a discussion of the normal-state scattering of the charge carriers off spin fluctuations. For the spin fluctuation spectral density $I^2\chi(\omega)$ we take a very simple model motivated in the work of Millis *et al.* [18] (MMP). We define a single characteristic spin fluctuation frequency $\omega_{\rm SF}$ and take

$$I^2\chi(\omega) = I^2 \frac{\omega/\omega_{\rm SF}}{\omega^2 + \omega_{\rm SF}^2}, \qquad (24)$$

where I^2 is a coupling constant which can be fit to normal-state infrared data based on Eq. (3) with $I^2\chi(\omega)$ playing the role of $\alpha^2F(\omega)$ in Eq. (5) for the self energy.

In Fig. 2 we show our result for $\tau_{\rm op}^{-1}(\omega)$ related to the conductivity by Eq. (7) for an optimally doped, twinned $YBa_2Cu_3O_{6.95}$ (YBCO) single crystal with $T_c = 92.4\,$K at temperature $T = 95\,$K. The solid curve is the data of Basov *et al.* [42]. The dashed and dotted curves are our best fits for $\omega_{\rm SF} = 10\,$meV and 30 meV, respectively, with I^2 adjusted to get the correct absolute value of the scattering rate at $T = 95\,$K and low energies ω. We see that both values of $\omega_{\rm SF}$ do not give equally satisfactory fits to the data. The dash-dotted curve, however, fits the data well and corresponds to $\omega_{\rm SF} = 20\,$meV. This fit provides us with a model $I^2\chi(\omega)$ valid for the normal-state of YBCO. A plot of this function is shown in Fig. 3 as the gray solid squares. Also shown in this figure are two sets of theoretical results based on the $I^2\chi(\omega)$ with $\omega_{\rm SF} = 20\,$meV which serve to illustrate the inversion technique. The experimental data on $\tau_{\rm op}^{-1}(\omega)$ gives the model $I^2\chi(\omega)$ spectrum. Next this model spectrum is used in the normal-state conductivity Eq. (3) and two temperatures are considered, namely $T = 95\,$K (dotted curve) and $T = 10\,$K (solid curve). Except for some numerical noise it is clear that when $W(\omega)$ (solid curve) is computed from Eq. (8) which involves a second derivative of our calculated data for $\tau_{\rm op}^{-1}(\omega)$ computed from the conductivity according to Eq. (7), that the low temperature data ($T = 10\,$K) gives a remarkable accurate picture of the input $I^2\chi(\omega)$ function and that to a very good approximation $W(\omega)$ is the same as $I^2\chi(\omega)$ in this case. If the temperature is increased to 95 K the match between $W(\omega)$ (dotted curve) and $I^2\chi(\omega)$ is not quite as good. This shows that our inversion technique summarized in Eqs. (7) and (8) is best when applied at low temperatures. The resultant inverted $I^2\chi(\omega)$ gets smeared somewhat if high temperatures are used instead.

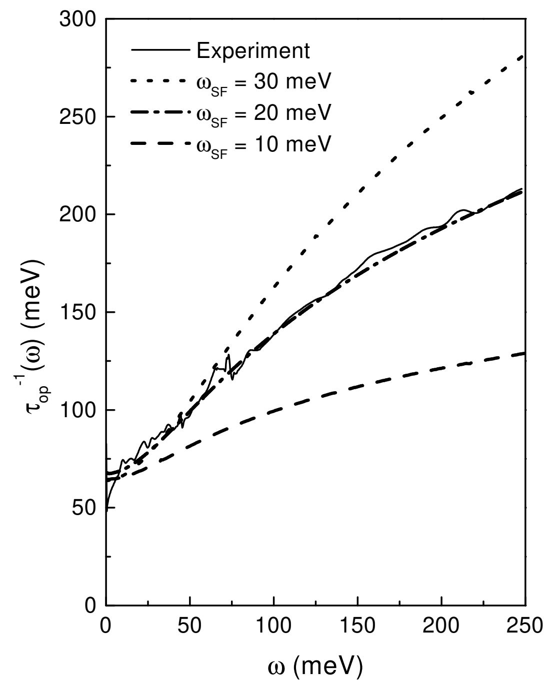

Fig. 2. The normal-state optical scattering rate $\tau_{\rm op}^{-1}(\omega)$ *vs.* ω for YBCO with a $T_c = 92.4\,$K obtained from the work of Basov *et al.* [42] (solid line) at a temperature of 95 K. The dash-dotted curve from theory based on Eq. (3) with an MMP model spectral density using a spin fluctuation frequency $\omega_{\rm SF} = 20\,$meV gives good agreement while the other choices of 30 meV (dotted line) or 10 meV (dashed line) do not.

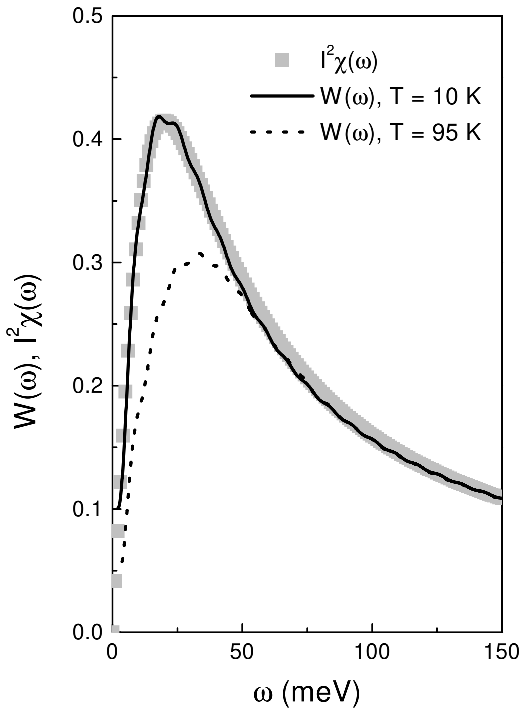

Fig. 3. Comparison of the spectral density $I^2\chi(\omega)$ (gray solid squares) in the MMP model [18] ($\omega_{\rm SF} = 20\,$meV) with the function $W(\omega)$ defined in Eq. (8) from the normal-state conductivity scattering rate Eq. (7). The solid curve is at $T = 10\,$K while the dotted curve is at 95 K.

2. The Superconducting State, $I^2\chi(\omega)$ and the Infrared Conductivity

Going to the superconducting state requires the solution of the Eliashberg equations (13) and evaluation of formula (17) for the optical conductivity. This is much more complicated than the corresponding normal-state analysis. Also, it is critical to understand that since we are dealing with a highly correlated system and the excitations we are exchanging in our spectral density are within the electronic system itself, they could be profoundly modified by the onset of the transition. In Fig. 4 we reproduce spin polarized inelastic neutron scattering results of the spin fluctuations measured in a sample of $YBa_2Cu_3O_{6.92}$ by Bourges *et al.* [43] at two temperatures namely $T = 100$ K (open squares) and $T = 5$ K (solid circles) which show the formation of the 41 meV spin resonance in the superconducting state. At 100 K the measured spectrum looks very much like the simple spectrum used in our analysis of the optical data in YBCO (Fig. 3) but this simple form is profoundly modified in the superconducting state with the imaginary part of the magnetic susceptibility depressed at small ω and the formation of a sharp peak around $E_r = 41$ meV. The possibility of a change in $I^2\chi(\omega)$ brought about by the onset of superconductivity must be included in our analysis of the optical data in the superconducting state. A question we can immediately ask is: is the 41 meV peak seen in optimally doped YBCO in neutron scattering also seen in the superconducting state optical conductivity? To perform the necessary analysis several modifications of what has been done so far need to be considered. The observation that, in the normal-state the well defined function $W(\omega)$ given in Eq. (8) which is easily accessible when the conductivity $\sigma(\omega)$ is known, can be identified to a good approximation with $I^2\chi(\omega)$ may not hold in the superconducting state of a d-wave superconductor.

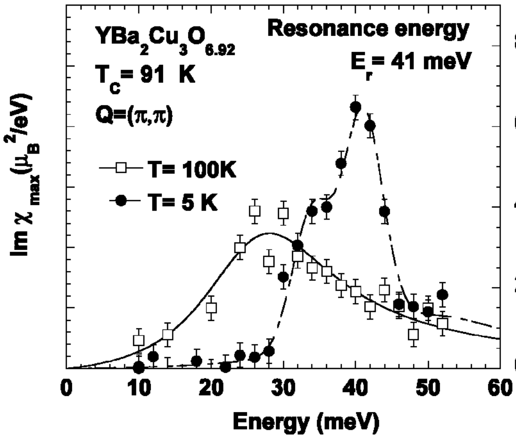

Fig. 4. Experimental results of the magnetic susceptibility at $\mathbf{Q} = (\pi, \pi)$ in a sample of $YBa_2Cu_3O_{6.92}$. The imaginary part of χ is measured as a function of energy. Open squares are results at $T = 100$ K and solid circles are at $T = 5$ K (in the superconducting state, $T_c = 91$ K for this sample). The energy of the spin resonance $E_r = 41$ meV. Adapted from [43].

It turns out from extensive calculations of the superconducting state conductivity based on Eqs. (17) by Schachinger and Carbotte [44,45] that a simple modification of the rule

$$I^2\chi(\omega) \simeq W(\omega)$$

can be found which applies approximately in the superconducting state in the resonance region, namely

$$I^2\chi(\omega_1) \simeq \frac{W(\omega_2)}{2},$$

with ω_2 shifted by $\Delta_0(T)$, the energy gap at temperature T, when compared with ω_1. This rule, while not exact, is nevertheless sufficiently accurate to make it useful in obtaining first qualitative information on the magnitude and frequency dependence of the underlying charge carrier — exchange boson interaction spectral density from optical data. We expect the changes in going to the superconducting state to be the growth of the resonance, while at higher energies there should be no change in $I^2\chi(\omega)$ from its normal state value. A detailed comparison of $I^2\chi(\omega)$ and $W(\omega)$ in the superconducting state will be given later when we relate additional structures in $W(\omega)$ not in $I^2\chi(\omega)$ to structures in the superconducting quasiparticle density of states which introduce distortions in $W(\omega)$ as compared to the underlying spectral density. In Fig. 5 we show results for the case of YBCO [25,46] at $T = 10$ K. The solid line was obtained directly from differentiation of experimental data on the optical scattering rate using the superconducting state conductivity $\sigma(\omega)$ in Eq. (7) and the definition (8) of $W(\omega)$. It is limited to the resonance region. It shows that $W(\omega)/2$ clearly has a peak corresponding to the peak seen in the spin susceptibility of Fig. 4 measured in neutron scattering. Of course, $I^2\chi(\omega)$ includes the coupling constant I^2 between electrons and spin fluctuations and is not strictly the imaginary part of the spin susceptibility. These two functions are not the same but we do know that an optical resonance peak does appear when the neutron peak is observed. They fall at the same frequency E_r and look similar in other aspects. It is important to emphasize that this solid curve comes directly from the data on $\sigma(\omega)$ and can be interpreted as evidence for coupling of the charge carriers to the spin one resonance at 41 meV. The other curves in the figure are equally important. The gray squares represent the $I^2\chi(\omega)$ used in calculations displaced in energy by the gap $\Delta_0 = 27$ meV. It is constructed completely from experiment. The fitting procedure involves two critical independent steps. First the data on $\tau_{\rm op}^{-1}(\omega)$ in the normal-state is used to get a background spectrum of the form given in Eq. (24) which applies to the normal-state. This defines $\omega_{\rm SF}$ and the corresponding I^2. This spectrum is also valid at the critical temperature T_c. We use this to determine the last parameter, the anisotropy parameter g in Eqs. (10a) and (13a), in solving the linearized Eqs. (10) for g to give the required T_c. In the second step the normal-state result for the spectral density is modified only in the region of the resonance peak leaving it unchanged at higher energies. The resonance is positioned and its magnitude given by the data for the experimental $W(\omega)/2$ (solid curve). There is no ambiguity and the procedure is definite. A check on the consistency of this procedure is then performed in calculating the theoretical $W(\omega)/2$ (dashed line) from the theoretical optical scattering rate calculated numerically from the solutions of the Eliashberg equations. We see that the theoretical data agree remarkably well with experiment in the region of the resonance. More explanations of the differences between $W(\omega)/2$ and $I^2\chi(\omega)$ beyond the resonance region will be provided later on.

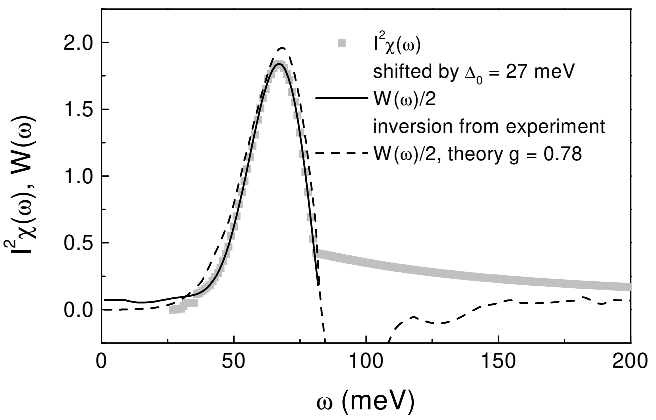

Fig. 5. The model charge carrier spin excitation spectral density $I^2\chi(\omega)$ for $T = 10\,\mathrm{K}$ (gray solid squares) constructed from conductivity data for optimally doped YBCO. The dashed line which follows the gray solid squares faithfully, except for negative oscillations just beyond the spin resonance around 68 meV, is $W(\omega)/2$ obtained from our model $I^2\chi(\omega)$ (displaced by the gap energy $\Delta_0 = 27\,\mathrm{meV}$ in the figure). The solid line is the coupling to the resonance found directly from experiment.

After this important low temperature consistency check we can now study in more detail the temperature dependence of the spectral density $I^2\chi(\omega)$ in the superconducting state of an optimally doped, twinned YBCO single crystal using experimental data. The frequency dependence of the optical scattering rate has been studied at five temperatures by Basov *et al.* [42]. We reproduce their experimental results in the top frame of Fig. 6. The data are for $T = 10\,\mathrm{K}$ solid line, $T = 40\,\mathrm{K}$ dotted line, $T = 60\,\mathrm{K}$ dashed line, $T = 80\,\mathrm{K}$ dash-dotted line, and $T = 95\,\mathrm{K}$ (in the normal-state) gray solid line. We see that in the normal-state $\tau_{\mathrm{op}}^{-1}(\omega)$ *vs.* ω shows a quasi-linear dependence on ω but in all other curves a depression below the normal curve is seen at small ω below roughly 75 meV. The depression is the more pronounced the lower the temperature. At higher frequencies all curves roughly coincide. At low temperatures, $\tau_{\mathrm{op}}^{-1}(\omega)$ as a function of ω shows a small value up to 50 meV or so, with a sharp rise around 75 meV characteristic of the existence of a sharp peak in $I^2\chi(\omega)$. It is clear that this peak increases in strength as T is lowered into the superconducting state. More quantitative information on the temperature variation of the optical resonance, its strength in $I^2\chi(\omega)$, and its position is shown in the bottom frame of Fig. 6 where we show the second derivative $W(\omega)$ function derived directly from the data given in the top frame by performing the differentiation indicated in Eq. (8). The solid curve is for $T = 10\,\mathrm{K}$, the dotted curve for $T = 40\,\mathrm{K}$, the dashed for $T = 60\,\mathrm{K}$, and dash-dotted for $T = 80\,\mathrm{K}$. The height of the peak of the resonance clearly increases with lowering of the temperature. In the curves for $W(\omega)$ *vs.* ω the position of the peak is seen to be reduced as T is increased towards T_c. If it is remembered that the peak in $W(\omega)$ is located at the gap value $\Delta_0(T)$ plus the position of the resonance E_{r} and the temperature dependence of the gap is accounted for (it decreases with increasing temperature and rapidly goes to zero as T_c is approached) then we conclude that the position of the resonance is temperature independent although its strength decreases as T increases. This is also in agreement with the observation made by Dai *et al.* [47] that the energy at which the spin one resonance is observed in YBCO (41 meV) is temperature independent.

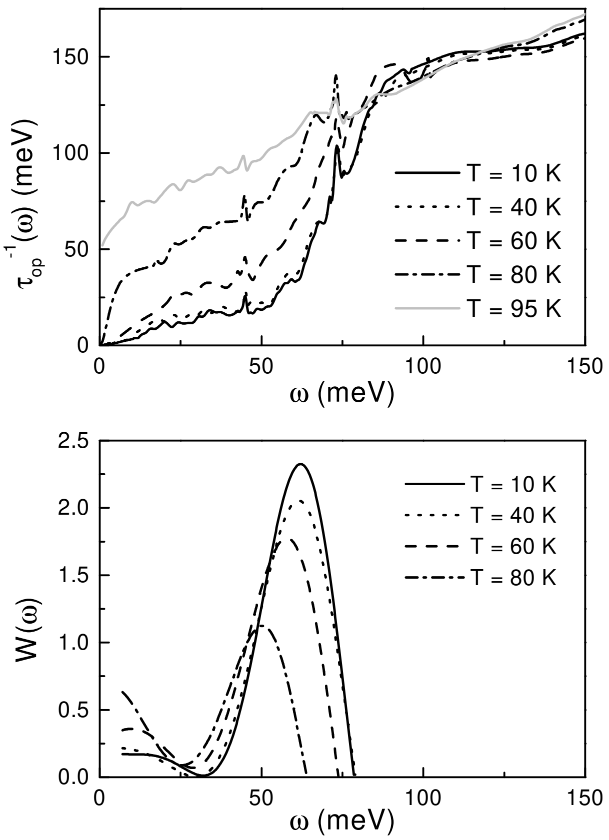

Fig. 6. Top frame: optical scattering rate $\tau_{\mathrm{op}}^{-1}(T,\omega)$ in meV for optimally doped, twinned YBCO single crystals [42]. Bottom frame: function $W(\omega)$ *vs.* ω in the region of the optical resonance.

In Fig. 7 we show results for the spectral density $I^2\chi(\omega)$ *vs.* ω obtained from the data of Fig. 6 at five temperatures, namely $T = 95\,\mathrm{K}$ (solid gray curve), $T = 80\,\mathrm{K}$ (dash-dotted curve), $T = 60\,\mathrm{K}$ (dashed curve), $T = 40\,\mathrm{K}$ (dotted curve), and $T = 10\,\mathrm{K}$ (solid black curve). The procedure follows in all cases the procedure already described in detail for the $T = 10\,\mathrm{K}$ data. Now, the resonance is positioned and its magnitude given by the $W(\omega)$ data shown in the bottom frame of Fig. 6 and $W(\omega)/2$ is used to modify the normal-state MMP background spectrum only in the region of the resonance.

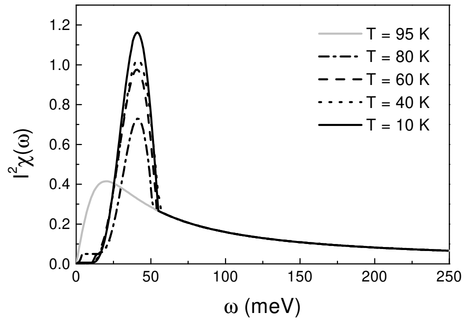

Fig. 7. The charge carrier-spin excitation spectral density $I^2\chi(\omega)$ determined from optical scattering data at various temperatures. Solid gray curve $T = 95\,\mathrm{K}$, dash-dotted $T = 80\,\mathrm{K}$, dashed $T = 60\,\mathrm{K}$, dotted $T = 40\,\mathrm{K}$, and black solid $T = 10\,\mathrm{K}$. Note the growth in strength of the $41\,\mathrm{meV}$ optical resonance as the temperature is lowered.

A consistency check is then performed for all temperatures and we present the $T = 40\,\mathrm{K}$ result in Fig. 8. The top frame gives $W(\omega)/2$ obtained directly from experiment in the resonance region (solid line, corresponds to the dotted line in the bottom frame of Fig. 6). The model $I^2\chi(\omega)$ for this temperature is given by the gray solid squares displaced in energy by the superconducting gap $\Delta_0 = 21\,\mathrm{meV}$. This spectrum agrees with the experimental $W(\omega)/2$ in the resonance region. The dashed curve, finally, represents the theoretical $W(\omega)/2$ and we recognize, again, a remarkable agreement between theory and experiment in the appropriate energy range. The fit to the optical scattering rate which in the end is the quantity that matters is shown in the bottom frame of Fig. 8. The theoretical curve (dashed line) follows well the experimental data (solid line). In this sense we have found a spectral density which can reproduce the measured optical scattering rate at $T = 40\,\mathrm{K}$ and it does not matter much how we arrived at our final model for $I^2\chi(\omega)$ which involved, as a step, consideration of the function $W(\omega)$ which served to guide our choice.

We return now to a more detailed discussion of the optical conductivity. In Fig. 9 we show the real part of the optical conductivity $\sigma_1(\omega)$ for untwinned, optimally doped YBCO single crystals (solid line) reported by Homes *et al.* [48] and compare with results of various calculations. This means that we are now comparing theoretical predictions with experimental YBCO data which have not been used to derive the $I^2\chi(\omega)$ spectra. The gray solid curve is the BCS result for a gap of $24\,\mathrm{meV}$ and impurity scattering in Born approximation corresponding to $t^+ = 0.32\,\mathrm{meV}$. It is very clear that no agreement with experiment is possible with BCS d-wave. One needs to go to an Eliashberg formulation if one is to even get close to the data. In some sense this is very positive since a good fit with a BCS formulation would mean that details of the pairing potential do not play an important role in the conductivity and, thus, our procedure would not be a good way to pin down some of the details of the pairing interaction. The dash-dotted curve represents results of Eliashberg calculations but with an MMP model for the $I^2\chi(\omega)$ kernel. This ignores the growth of the $41\,\mathrm{meV}$ optical resonance that enters when the superconducting state develops. While the agreement with the data is good at high energies beyond $100\,\mathrm{meV}$ say, it fails completely in the low energy region. In particular, the Drude like peak at very low energies is much too narrow. It is important, however, to emphasize the difference between Eliashberg and BCS at high energies where BCS gives a conductivity which is much too small while, in comparison, Eliashberg with an MMP kernel gives larger values reflecting the long tails extending to $400\,\mathrm{meV}$ in the MMP $I^2\chi(\omega)$ spectrum. This is taken as strong evidence for the existence of long tails in the pairing spectral density and argues against a pure phonon mechanism which would be lot more confined in energy.

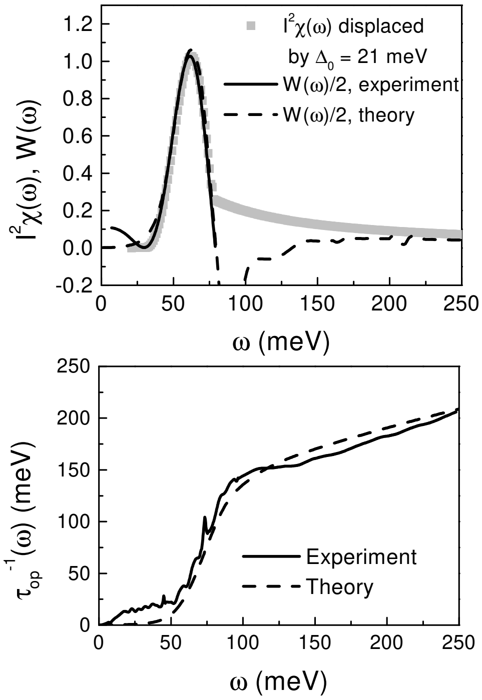

Fig. 8. The top frame gives the resonance peak obtained directly from the optical data for YBCO in the superconducting state (solid curve) at $T = 40\,\mathrm{K}$, the model $I^2\chi(\omega)$ (gray squares) displaced by the gap, and the theoretical results for $W(\omega)/2$ obtained from the model spectral density (dashed line). The bottom frame gives the optical scattering rate $\tau_{\mathrm{op}}^{-1}(\omega)$ *vs.* ω. The experimental results give the solid curve and our theoretical fit to it is the dashed curve.

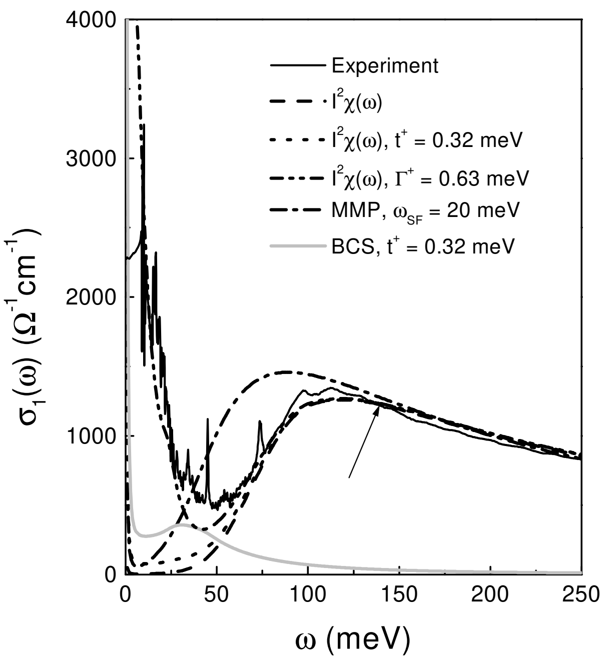

Fig. 9. Comparison of the real part of the in-plane conductivity $\sigma_1(\omega)$ *vs.* ω for various models ($T = 10$ K). The grayed solid line with a peak before 50 meV is BCS. The dash-dotted line is an Eliashberg calculation with an MMP spectral density peaked at $\omega_{\rm SF} = 20$ meV. The dashed line is the same but with our temperature and frequency dependent $I^2\chi(\omega)$ (see Fig. 7) used instead of the MMP model. As described in the text this charge carrier — exchange boson interaction spectral density $I^2\chi(\omega)$ has been determined through a consideration of in-plane optical data. The dotted (Born) and dash-double-dotted (unitary scattering) curves include impurities in addition to the $I^2\chi(\omega)$ model for inelastic scattering. The solid line is the data of Homes *et al.* [48].

The dashed curve in Fig. 9 gives our results for the real part of the conductivity $\sigma_1(\omega)$ when our $I^2\chi(\omega)$ at $T = 10$ K (solid line in Fig. 7) is used in the calculations rather than the MMP kernel. The existence of the 41 meV resonance shifts the large rise in the conductivity which now begins at much higher energies ~ 50 meV than in the MMP case. It also leads to a maximum around 100 meV in good agreement with experiment. Even better agreement can be obtained if a small amount of impurity scattering is included within the unitary or resonant scattering limit $c \to 0$ in Eq. (13). Results with $\Gamma^+ = 0.63$ meV are shown as the dash-double-dotted curve which displays all the important characteristics observed in the experimental data. The agreement is truly very good. A final curve including only Born impurity scattering (dotted curve) shows that this limit cannot explain the data. It should be clear from this comparison that BCS theory is quite inadequate in describing the observed features of the real part of the infrared conductivity as a function of frequency while Eliashberg theory can give a good fit. It is also clear that some impurity scattering in the unitary limit is needed and that the electron–boson exchange spectral density has long tails extending to at least 400 meV, and at $T = 10$ K has a large contribution from the 41 meV resonance peak.

In Fig. 10 we show our results for the imaginary part of the optical conductivity $\sigma_2(\omega)$. What is plotted is $\omega\sigma_2(\omega)$ *vs.* ω at $T = 10$ K. The solid curve gives data from Homes *et al.* [48]. The dash-dotted curve are Eliashberg results based on an MMP kernel which does not account for charge carrier coupling to the 41 meV resonance. It fails to reproduce the data. On the other hand, when the resonance is included in our $I^2\chi(\omega)$ we get the dashed curve which agrees with the data much better and shows a large depression in the curve located around 75 meV in agreement with the data. This is the signature in $\sigma_2(\omega)$ of the 41 meV resonance in $I^2\chi(\omega)$. At very low energies the agreement is not as good. As for the real part of the conductivity this region is sensitive to impurity scattering while at higher energies only inelastic scattering is really important. The dash-double-dotted curve includes impurities in the unitary limit with $\Gamma^+ = 0.63$ meV as before. This produces excellent agreement with the data even in the small ω region which is not as well described in the case of Born scattering (dotted curve with $t^+ = 0.32$ meV). It is clear from this graph that $\omega\sigma_2(\omega)$ has an easily identifiably signature of the spin resonance. Also, the spectral density extends to high energies and Eliashberg theory with some contribution from unitary scattering impurities is in very good agreement with the data.

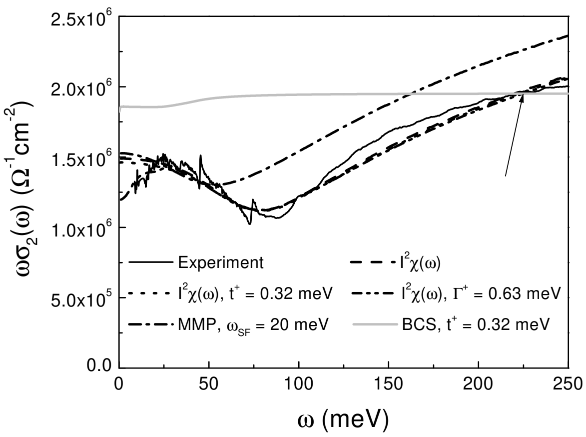

Fig. 10. The imaginary part of the conductivity $\omega\sigma_2(\omega)$ *vs.* ω for the various models described in Fig. 9 ($T = 10$ K). The solid curve is the data [48]. The dash-dotted curve is the result of an Eliashberg calculation with an MMP model while the other curves are based on the model $I^2\chi(\omega)$ which includes the 41 meV resonance. These three curves are for the pure case (only inelastic scattering, dashed line), the others are with some additional elastic impurity scattering in Born (dotted) and unitary (dash-double-dotted) limit with $t^+ = 0.32$ meV and $\Gamma^+ = 0.63$ meV respectively. The gray solid line is the BCS result.

While we have seen that an unmistakable signature of the 41 meV optical resonance exists in the data on both real and imaginary part of the infrared conductivity as a function of energy ω in the $T = 10$ K data, the resonance is even clearer in the second derivative defined by $W(\omega)$ of Eq. (8). The near equality between $W(\omega)$ and $\alpha^2F(\omega)$ established by Marsiglio *et al.* [24] for a phonon mechanism was only for the normal-state, i.e.: $\tau_{\rm op}^{-1}(\omega)$ entering the formula is the normal-state optical scattering rate. But in the high T_c cuprates the only low temperature data available is often in the superconducting state. Thus, we need to discuss in more detail what happens in Eq. (8) when $\tau_{\rm op}^{-1}(\omega)$ is replaced by its superconducting state value. As we have seen in Fig. 3, in the normal-state and at low temperatures $W(\omega)$ is almost exactly [25,44,45,49,50] equal to the input $I^2\chi(\omega)$ for models based on the NAFFL. Of course, $I^2\chi(\omega)$ is seen in $W(\omega)$ through electronic processes. But in the normal-state the electronic density of states $N(\varepsilon)$ is constant in the important energy region and, thus, does not lead to additional structures in $W(\omega)$ that are not in $I^2\chi(\omega)$. Such additional structures would then corrupt the signal, if the aim is to obtain $I^2\chi(\omega)$ from $W(\omega)$. This is no longer the case in the superconducting state because of the logarithmic van Hove singularities in $N(\varepsilon)$ and these do indeed strongly influence the shape of $W(\omega)$ and introduce additional structures in $W(\omega)$ corresponding to combinations of the positions of the singularity in $N(\varepsilon)$ and the peak in $I^2\chi(\omega)$ at $E_{\rm r}$ as described by Abanov *et al.* [51].

The structures in $W(\omega)$ corresponding to these singularities contaminate the signal in the sense that $W(\omega)$ in the superconducting state is no longer equal to the input $I^2\chi(\omega)$ [44,45]. In fact, only the resonance peak appears clearly at $\Delta_0 + E_{\rm r}$ and its size in $W(\omega)$ is about twice the value of $I^2\chi(\omega)$ at that frequency. In some cases the tails in $W(\omega)$ also match well the tails in $I^2\chi(\omega)$. In the end, of course, $W(\omega)$ serves only as a guide and it is the quality of the final fit to the conductivity data that determines the quality of the derived $I^2\chi(\omega)$.

Nevertheless, besides giving a measure of the coupling of the charge carriers to the optical resonance $W(\omega)$ can also be used to see the position of density of states singularities, as shown in Fig. 11 where $I^2\chi(\omega)$ (gray squares) and $W(\omega)$ (solid line) derived from our theoretical results are compared. Also shown by vertical arrows are the positions of $\Delta_0 + E_{\rm r}$, $2\Delta_0 + E_{\rm r}$, $\Delta_0 + 2E_{\rm r}$, and $2\Delta_0 + 2E_{\rm r}$. We note structures at each of these places and this information is valuable. Note that at $2\Delta_0 + E_{\rm r}$ the large negative oscillation seen in $W(\omega)$ is mainly caused by the kink in $I^2\chi(\omega)$ (gray squares) at about 75 meV. The density of electronic states effects clearly distorted the spectrum above the resonance peak and $W(\omega)$ stops agreeing with the input $I^2\chi(\omega)$ in this region until about 150 meV where agreement is recovered. In summary, $W(\omega)$ contains some information on singularities in $N(\varepsilon)$ as well as on the shape and size of $I^2\chi(\omega)$ and, in the superconducting state, the two effects cannot be clearly separated. Nevertheless, $W(\omega)$ remains a valuable intermediate step in the construction of a charge carrier — exchange boson interaction spectral density from optical data. To close, the dashed curve in Fig. 11 is the direct experimental data for $W(\omega)/2$ which is remarkably similar to theory when we consider that a second derivative is needed to get this curve.

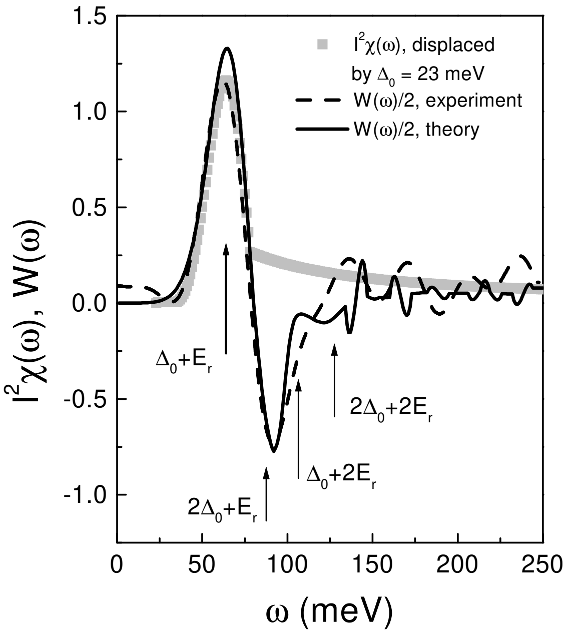

Fig. 11. Second derivative $W(\omega)$ compared with the input spectral density $I^2\chi(\omega)$. The 41 meV peak in $I^2\chi(\omega)$ (gray squares) is clearly seen in $W(\omega)/2$ (solid line) as are the tails at higher energies. In the energy region between 75 and 150 meV the van Hove singularities in the electronic density of states show up added on to E_r and distort the correspondence between $W(\omega)/2$ and $I^2\chi(\omega)$. The dashed line shows the function $W(\omega)/2$ derived from experimental data.

Next we want to concentrate on the out-of-plane conductivity (c-axis conductivity) of YBCO. Before presenting results we stress that the boson exchange kernel $I^2\chi(\omega)$ is an in-plane quantity and is taken from our discussion of the in-plane conductivity. It is not fitted to any c-axis data. It is to be used unchanged to calculate the out-of-plane conductivity assuming first coherent hopping with $t_\perp(\mathbf{k}) = t_\perp\cos^2(\phi)$ in Eqs. (19). The solid curve in Fig. 12 is the in-plane Eliashberg result which is included for comparison with the dashed curve which is for the c-axis. In the boson assisted region, which would not exist in a BCS theory, both curves have a remarkably similar behavior. At very low frequencies, a region which comes mainly from the coherent delta function part of the carrier spectral density, and which is the only part included in BCS, we note a narrow Drude-like peak in the solid curve. This part is suppressed in the c-direction (dashed curve) because the contribution from the nodal quasiparticles are effectively left out by the $t_\perp\cos^2(\phi)$ weighting term. Also, shown for comparison are BCS results for coherent hopping (dotted curve) along the c-axis. These results show no resemblance to our Eliashberg results and also do not agree with experiment Fig. 13. What determines the main rise in the region beyond the Drude part of the conductivity in $\sigma_{1c}(\omega)$ are the boson assisted processes and this rise does not signal the value of the gap or twice the gap for that matter, but rather a combination of Δ_0 and the resonance energy $E_{\rm r}$.

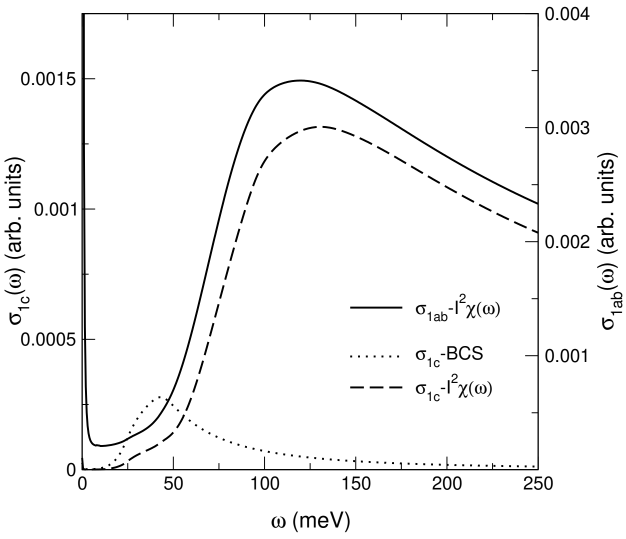

Fig. 12. Comparison between in-plane (solid line) and out of plane (dashed line) real part of the c-axis conductivity $\sigma_{1c}(\omega)$ *vs.* ω in an Eliashberg model with our model carrier-boson spectral density $I^2\chi(\omega)$ which includes the 41 meV spin resonance. The dotted curve is $\sigma_{1c}(\omega)$ for a BCS d-wave model with the same gap value as in the Eliashberg work and is included for comparison.

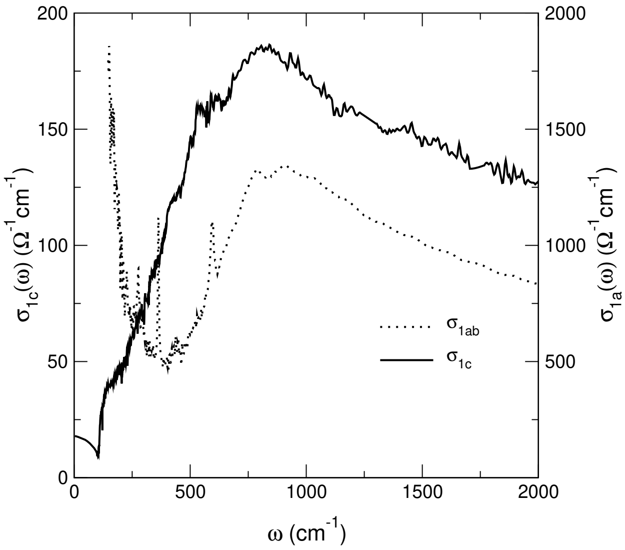

Fig. 13. Comparison between in-plane (dotted) and out of plane (solid) for the real part of the conductivity $\sigma_1(\omega)$ *vs.* ω. The data is from Homes *et al.* [48].

In Fig. 13 we compare the data of Homes *et al.* [48] on the same graph for in-plane (dotted) and out-of-plane (solid) conductivity $\sigma_1(\omega)$. It is clear that in the c-direction, the nodal quasiparticles seen in the dotted curve are strongly suppressed. This favors the $t_\perp \cos^2(2\phi)$ matrix element for the c-axis dynamics as we have just seen. Further, in the boson assisted region the two curves show almost perfect agreement with each other, which again favors the $t_\perp \cos^2(2\phi)$ coupling as was illustrated in the theoretical curves of Fig. 12. One difference is that the main rise, indicating the onset of the boson assisted incoherent (in-plane) processes, appears to have shifted slightly toward lower frequencies in the c-axis data as opposed to a shift to slightly higher frequencies in our theory. It should be remembered, however, that in the raw c-axis data, large structures appear in the conductivity due to direct phonon absorption and these need to be subtracted out, before data for the electronic background of Fig. 13 can be obtained. In view of this, it is not clear to us how seriously we should take the relatively small disagreements that we have just described between theory and experiment.

With the above reservation kept in mind we show in Fig. 14, a comparison of various theoretical results with experimental c-axis conductivity (black solid line). There are five additional curves. The black ones are obtained from an Eliashberg calculation based on the MMP model for $I^2\chi(\omega)$ with impurities $t^+ = 0.32$ meV included to simulate the fact that the samples used are not perfect, i. e.: are not completely pure, but this parameter does not play a critical role in this discussion. Incoherent c-axis coupling is assumed with $|V_1/V_0| = 1$ (black dotted). It is clear that this curve does not agree well with the data and that the coupling along the c-axis cannot be dominated by incoherent hopping between planes. This is also in agreement with the results of a theoretical study by Dahm *et al.* [52] who also observed better agreement for coherent c-axis conductivity in the overdoped regime. On the other hand the fit with the black dashed line is good in comparison. It uses the same MMP model but with coherent coupling of the form $t_\perp(\mathbf{k}) = t_\perp \cos^2(2\phi)$. This fit may already be judged satisfactorily but it should be remembered that if we had used the model of $I^2\chi(\omega)$ with the 41 meV peak included instead of MMP, the agreement would have deteriorated. This is troubling since one would expect that coupling to the 41 meV spin resonance would be stronger in the c-direction data than it is in the in-plane data. This is because the c-axis emphasizes the hot spots around the antinodal directions which connect best to (π, π) in the magnetic susceptibility. This is the position in momentum space where this spin resonance is seen to be located in optimally doped YBCO. On the other hand, recent ARPES data [23,53–55] which fit well the MFL (marginal Fermi liquid) phenomenology show little in-plane anisotropy for scattering around the Fermi surface and this is consistent with the findings here.

The dash-dotted curve in Fig. 14 illustrates a fit to the data that can be achieved with a dominant coherent piece and subdominant incoherent contribution. It is not clear to us whether such a close fit is significant given the uncertainties in the data and the lack of uniqueness in the fitting procedure. It does, however, illustrate the fact that a small amount of incoherent c-axis hopping cannot be completely ruled out from consideration of the infrared data and that this data can be understood quite well within Eliashberg theory. The last two curves (solid gray and dotted gray) are based on BCS d-wave theory and are reproduced here to illustrate the fact that such a theory is unable to explain the c-axis data. The solid gray curve is with $t_\perp(\mathbf{k}) = t_\perp \cos^2(2\phi)$ and the dotted gray one for incoherent c-axis transport. Compared with our Eliashberg results the agreement with the data is poor.

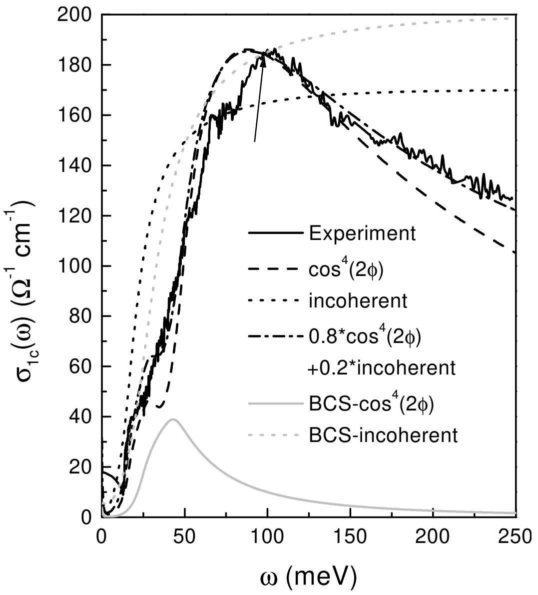

Fig. 14. Comparison with the data of Homes *et al.* [48] for the c-axis conductivity (black solid curve). The theoretical curves were obtained in a BCS theory, solid gray (coherent), dotted gray (incoherent) and the others in Eliashberg theory with MMP model and impurities $t^+ = 0.32\,\mathrm{meV}$. The black dotted curve is for incoherent c-axis with $|V_1/V_0| = 1$, the dashed for coherent c-axis with $t_\perp(\phi) = t_\perp \cos^2(2\phi)$ with ϕ an angle in the two dimensional CuO_2 Brillouin zone, and the dash-dotted is a fit to the data provided by a mixture of coherent and incoherent. We stress that this last fit is for illustrative purposes only, and is not unique.

3. The Microwave Conductivity

The microwave conductivity as a function of temperature in pure single crystals of YBCO revealed the existence of a very large peak around 40 K [20] whose size and position in temperature depends somewhat on the microwave frequency used. This peak has been widely interpreted as due to a rapid reduction in the inelastic scattering below T_c and is generally referred to as the collapse of the low-temperature inelastic scattering rate. This has been taken as strong evidence that the mechanism involved is electronic in origin and, this fact translates in our formalism into the fact, that the charge carrier — exchange boson interaction spectral density $I^2\chi(\omega)$ is reduced at low frequencies due to the onset of superconductivity. We have already seen in Fig. 7 the growth of the 41 meV resonance in $I^2\chi(\omega)$ as the temperature is lowered. At the same time the in-plane infrared optical data shows a gapping or at least a strong reduction of spectral weight at small ω. This implies that for temperatures smaller than the characteristic energy associated with this reduction, the inelastic scattering rates will become exponentially small and therefore the inelastic scattering time will become very large. This feature by itself will increase the microwave conductivity. At the same time the normal fluid density is of course decreasing towards zero. This feature reduces the absorption which is due only to the normal excitation. The two effects combine to give a maximum in the real part of the microwave conductivity at some intermediate temperature.

Another possible way to describe this collapse of the inelastic scattering time is the introduction of a temperature dependent inelastic scattering time which can be modeled from spin fluctuation theory [56].

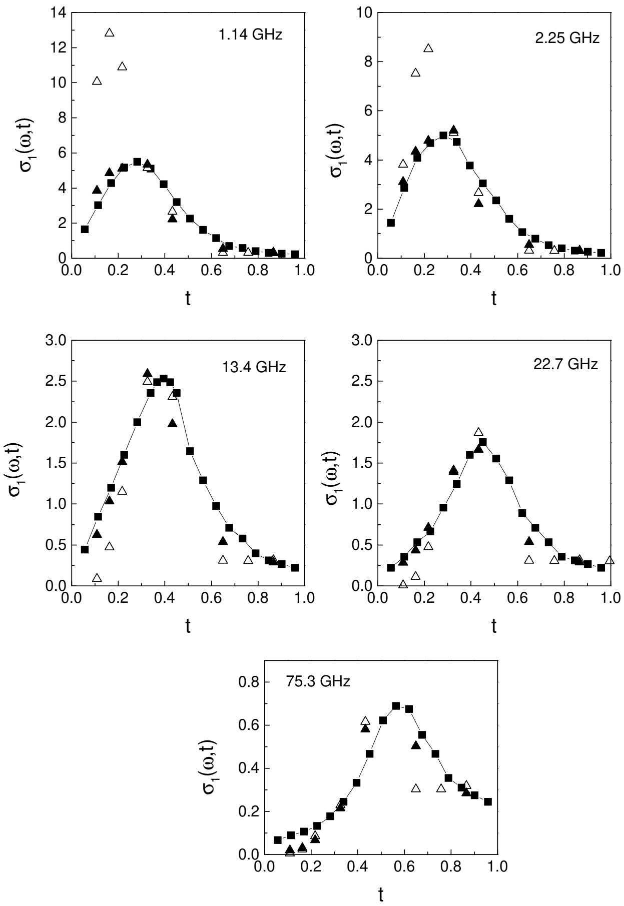

Fig. 15. Microwave conductivity $\sigma_1(\omega, t)$ in $10^7\,\Omega^{-1}\mathrm{m}^{-1}$ *vs.* the reduced temperature $t = T/T_c$ for the five frequencies measured in experimental work of Hosseini *et al.* [57] namely Ω = 1.14, 2.25, 13.4, 22.7, and 75.3 GHz (bottom frame). Solid squares are experiment, open triangles clean limit and solid triangles inelastic scattering plus impurities characterized by a potential with $\Gamma^+ = 0.003\,\mathrm{meV}$ and $c = 0.2$.

Recently Hosseini *et al.* [57] provided new microwave data at five different frequencies between 1 and 75 GHz on ultra pure samples of $YBa_2Cu_3O_{6.99}$ grown in $BaZrO_3$ crucibles. In Fig. 15 we show results obtained from our Eliashberg solutions and compare with experiment [58]. The solid squares are the data of Hosseini *et al.*, the open triangles are our numerical results in the clean limit, and the solid triangles include a small amount of impurities characterized by $\Gamma^+ = 0.003\,\text{meV}$ and $c = 0.2$. The figure has five frames one for each of the five microwave frequencies considered, namely 1.14, 2.25, 13.4, 22.7, and 75.3 GHz. We see that even for these ultrapure crystals, results obtained without including impurities do not agree well with the data at the lowest microwave frequencies considered and at the lowest temperatures. For example, in the case of the $\omega = 1.14$ and 2.25 GHz runs the predicted peak is much to high. The agreement, however, improves as the frequency of the microwave probe is increased. More importantly, when a small amount of impurity scattering with $c = 0.2$ is included, good agreement is obtained in all cases. The same data plotted in a different way shows better the dramatic improvement in the agreement with the data when impurities are included. This is demonstrated in Fig. 16 where we show the data for the microwave conductivity $\sigma_1(\omega)$ *vs.* ω at three different temperatures. The data are represented by solid squares, up-triangles and down-triangles for $T = 10\,\text{K}$, 15 K and 20 K respectively. The open symbols give the results of our Eliashberg calculations in the pure case and the solid gray symbols include impurities. The gray lines through the points are a guide for the eye. The agreement with the data in this last case is within experimental error and is acceptable. It is clear, that a small amount of elastic scattering needs to be included in the calculations to achieve good agreement.

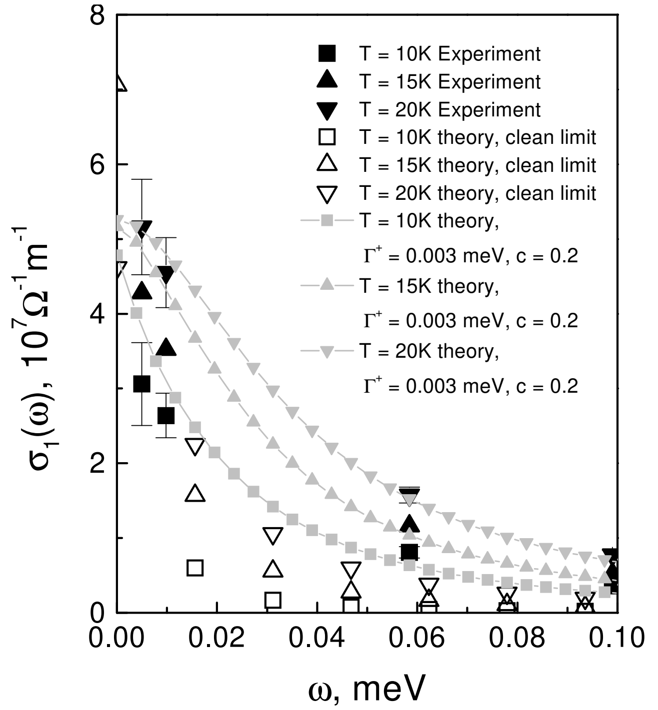

Fig. 16. The microwave conductivity $\sigma_1(\omega, T)$ as a function of ω for three different temperatures. The data is the same as shown in Fig. 15. The open symbols are theory for the pure limit, the solid gray symbols theory with some impurity scattering additionally included, and the solid black symbols are experiments. The squares are for $T = 10\,\text{K}$, the up-triangles for $T = 15\,\text{K}$, and the down-triangles for $T = 20\,\text{K}$.

We now turn to the c-axis. No new parameters relevant to the in-plane dynamics need to be introduced in order to understand the c-axis data. It is necessary, however, to have some model for the c-axis charge transfer. Coherent or incoherent hopping will lead to quite different conclusions as will the assumption, in the coherent hopping case, of a constant or a momentum dependent hopping probability. For the constant case the conductivity will mirror its in-plane value but its magnitude will of course be greatly reduced. For a θ-dependent matrix element, on the other hand, the nodal quasiparticles are eliminated from participation in the c-axis response and we can expect a behavior different from the in-plane results.

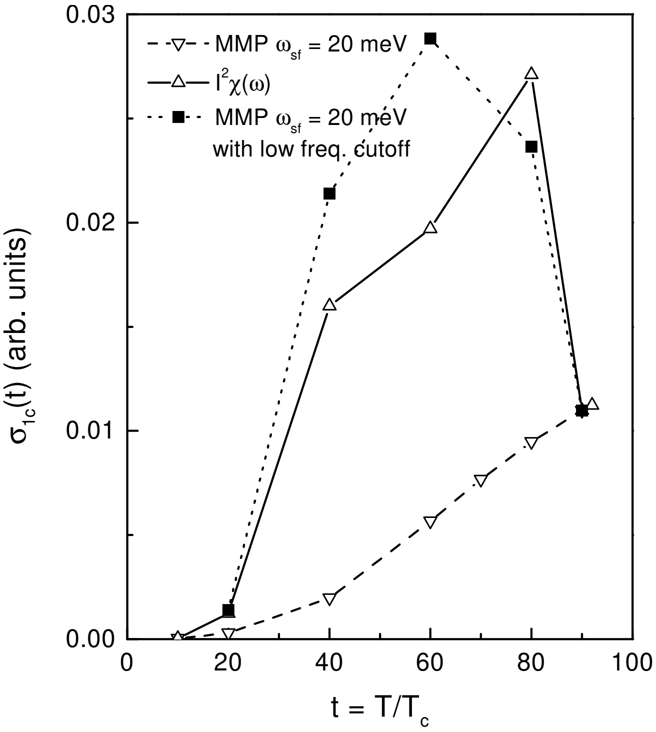

Fig. 17. The c-axis microwave conductivity $\sigma_{1c}(T)$ at $\omega = 22\,\text{GHz}$ as a function of temperature T. The open up-triangles were obtained from the empirically determined $I^2\chi(\omega)$ shown in Fig. 7. The solid squares are for an MMP form Eq. (19) with low frequency cutoff applied. This cutoff is the same as seen in Fig. 7. The open down-triangles employ the same MMP model with $\omega_{\text{SF}} = 20\,\text{meV}$ and without the low frequency cutoff. In this case there is no peak in $\sigma_{1c}(T)$. All curves are for coherent tunneling with $t_\perp(\mathbf{k}) = t_\perp \cos^2(2\theta)$.

In Fig. 17 we show numerical results for the temperature dependence of the real part of the c-axis microwave conductivity $\sigma_{1c}(T)$ at $\omega = 22\,\text{GHz}$ as a function of temperature T in arbitrary units. The results are for coherent hopping with a θ-dependent matrix element. For the in-plane case the same form applies except that the vertex $t_\perp(\mathbf{k})$ would be replaced by a Fermi velocity $v_{\mathbf{k}}$. In as much as both these vertices are taken to be independent of $\mathbf{k}$ they can be pulled out of the integral over $\mathbf{k}$ in Eqs. (19) and in-plane and out-of-plane conductivities differ only by a numerical constant which sets the over all scale in each case. Since no peak is observed in the temperature dependence of the c-axis conductivity [59] this case does not agree with experiment and will not be treated further here. Only results for $t_\perp(\mathbf{k}) = t_\perp \cos^2(2\theta)$ are considered in Fig. 17. The open up-triangles are the results obtained from the charge carrier — exchange boson interaction spectral density $I^2\chi(\omega)$ obtained empirically from the in-plane infrared conductivity (Fig. 7). This is the only material parameter which characterizes YBCO in the Eliashberg equations (13). Solutions of these equations determine the in-plane Green's function (22) and hence the c-axis conductivity Eqs. (21). Arbitrary units are used, so that the absolute value of $t_\perp$ is not required. We see a broad peak in $\sigma_{1c}(T)$ *vs.* T which is centered around $T = 60\,\mathrm{K}$ rather than around $T = 40\,\mathrm{K}$ for the in-plane case of Fig. 15. The c-axis peak is also smaller. These differences are entirely due to the extra factor of $\cos^4(2\theta)$ in the c-axis conductivity which eliminates the nodal direction. This has a profound effect on the resulting temperature dependence of $\sigma_{1c}(T)$ but, as we can see, does not entirely eliminate the peak in $\sigma_{1c}(T)$.

There is considerable disagreement with experiment which is shown as the solid squares in Fig. 18. Our theoretical results are robust in the sense that the peak is due to the greatly reduced spectral weight in $I^2\chi(\omega)$ of Fig. 7 at small ω when superconductivity sets in and this is fixed from consideration of the in-plane conductivity. The effect of this spectral weight reduction is further illustrated in Fig. 17 by the solid squares which employ instead of our empirical value for $I^2\chi(\omega)$ the simpler MMP form of Eq. (24) with the same low frequency cutoff as indicated in Fig. 7 being applied. The cutoff is of course temperature dependent and goes to zero at T_c.

The peak in $\sigma_{1c}(T)$ *vs.* T remains and is close to the results obtained when an optical resonance is included in addition to a low frequency cutoff. For comparison, the down-triangles were obtained when no low frequency cutoff was applied. We now see that the peak in $\sigma_{1c}(T)$ *vs.* T is completely eliminated. This demonstrates that the peak is due to the collapse of the inelastic scattering rate embodied in the low frequency gapping of the charge carrier-boson spectral density. In summary, even when a momentum dependent coherent hopping matrix element of the form $t_\perp(\mathbf{k}) = t_\perp \cos^2(2\theta)$ is considered, gaping of $I^2\chi(\omega)$ at small ω leads directly to a peak in the c-axis microwave conductivity. However, the spectral density $I^2\chi(\omega)$ which enters the Eliashberg equations (10) on the imaginary axis and (13) on the real axis could depend on position on the Fermi surface. This complication was not considered here but it is important to point out that coherent c-axis tunneling could lead to reasonable agreement with the measured temperature variation of the microwave conductivity, if the spectral density $I^2\chi(\omega)$ is different along the antinodal direction and, in particular, has no gapping at low frequencies. This difference might not have been picked up in our analysis of the in-plane conductivity which is characteristic of an average over all points on the Fermi surface and not just of the antinodal direction.

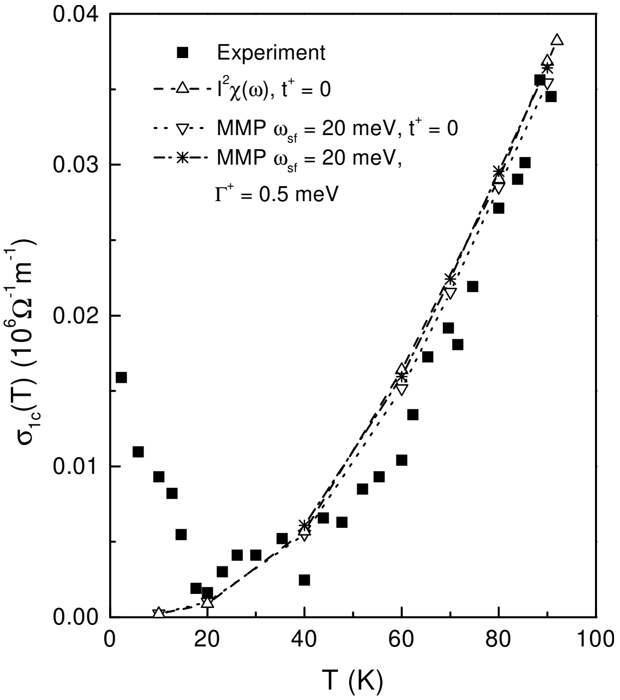

Fig. 18. The c-axis microwave conductivity $\sigma_{1c}(T)$ at $\omega = 22\,\mathrm{GHz}$ as a function of temperature T. The solid squares are the experimental results by Hosseini *et al.* [59] shown for comparison. The others are theory based on various models for the charge carrier — exchange boson interaction spectral density. All calculations are for the incoherent case based on Eqs. (21) with $V_1 = V_0$ in (22) and V_0 adjusted to match the experimental value at $T = 90\,\mathrm{K}$. Open up-triangles are based on our empirically determined charge carrier — exchange boson interaction spectral density $I^2\chi(\omega)$ of Fig. 7 without additional impurity scattering (pure limit). The open down-triangles are also in the pure limit but the MMP model (24) is used without cutoff. The stars are the same as the open down-triangles but now impurity scattering is included in the unitary limit with $\Gamma^+ = 0.5\,\mathrm{meV}$.

Fig. 18 shows results for the temperature variation of the c-axis microwave conductivity $\sigma_{1c}(T)$ at $\omega = 22\,\mathrm{GHz}$ in the incoherent coupling case, Eqs. (21). As we have indicated in Sec. 2 this formula involves a double integral over momentum which separately weights the two Green's functions. For simplicity, we show results only for the case $V_1 = V_0$ in the impurity model potential of Eq. (22). Other values have been considered but this does not change qualitatively any of the conclusions we will make. The open up-triangles give results when the empirical $I^2\chi(\omega)$ of Fig. 7 is used. We see that in this case the theory predicts no peak in $\sigma_{1c}(T)$ *vs.* T in good agreement with the experimental results of Hosseini *et al.* [59] (solid squares). The low frequency cutoff built into our $I^2\chi(\omega)$ (open up-triangles) has little effect on the resulting $\sigma_{1c}(T)$. This is verified directly when we compare with the open down-triangles which were obtained with the MMP form (24) without cutoff. These results differ very little from the previous ones and show that the application of a low frequency cutoff does not play a critical role for the incoherent case. This is in sharp contrast to the coherent case in which the low frequency cutoff leads directly to a peak in $\sigma_{1c}(T)$. The curves are also robust to the introduction of some elastic impurity scattering as is demonstrated with the final set of results in Fig. 18, denoted by stars, which is based on an MMP model with elastic impurity scattering included in the unitary limit with $\Gamma^+ = 0.5\,\mathrm{meV}$ in Eq. (11). We see that the inclusion of impurities does not appreciably change our results. The calculation clearly shows that the observed data can be understood naturally in an incoherent c-axis transport model and that the results are robust to changes in cutoff at low ω and to the addition of impurities.

This contrasts with the case of the c-axis infrared data which we described previously and found to support coherent rather than incoherent c-axis charge transfer.

4. Other Superconducting State Properties

The temperature dependence of the area under the spin resonance seen at (π, π) by spin polarized neutron scattering [47] has been measured and its temperature dependence denoted by $\langle m^2_{\mathrm{res}}(T)\rangle / \langle m^2_{\mathrm{res}}(T = 10\,\mathrm{K})\rangle$ is reproduced in the top frame of Fig. 19 as the solid circles. Also shown on the same plot are our results for the area under the optical resonance in our spectral density $I^2\chi(\omega)$ at various temperatures (see Fig. 7). We denote this by $A(T)$ and plot as the solid line the ratio $A(T)/A(T = 10\,\mathrm{K})$ which follows the same temperature variation as the neutron result. This temperature variation is also close to that of the gap edge shown as the dashed curve. This last curve was found as a byproduct of our Eliashberg calculations based on the numerical solutions of Eqs. (13). The gap amplitude at temperature T is given by $\Re\mathrm{e}\{\Delta(\omega = \Delta_0; T)\} = \Delta_0(T)$. The same solutions give the temperature dependence of the penetration depth and of the thermodynamic critical field which we present in the bottom frame of Fig. 19. The solid curve gives results for $[\lambda(0)/\lambda(T)]^2$ *vs.* $t = T/T_c$ (the reduced temperature) which are close to the experimental results of Bonn *et al.* [4] given as solid squares.

Further results are shown in Fig. 20 for the electronic part of the thermal conductivity as a function of temperature. It shows, as does the in-plane microwave conductivity, a large peak around 40 K. The solid triangles are the results of our calculations while the solid squares are the experimental results of Matsukawa *et al.* [60]. The agreement is remarkably good. We stress that no adjustable parameters enter our calculations except for a choice for the impurity parameter t^+ which is also restricted in this particular case because t^+ has already been determined by a previous fit to the microwave data [15]. The kernel in the Eliashberg equations is completely determined from optical data.

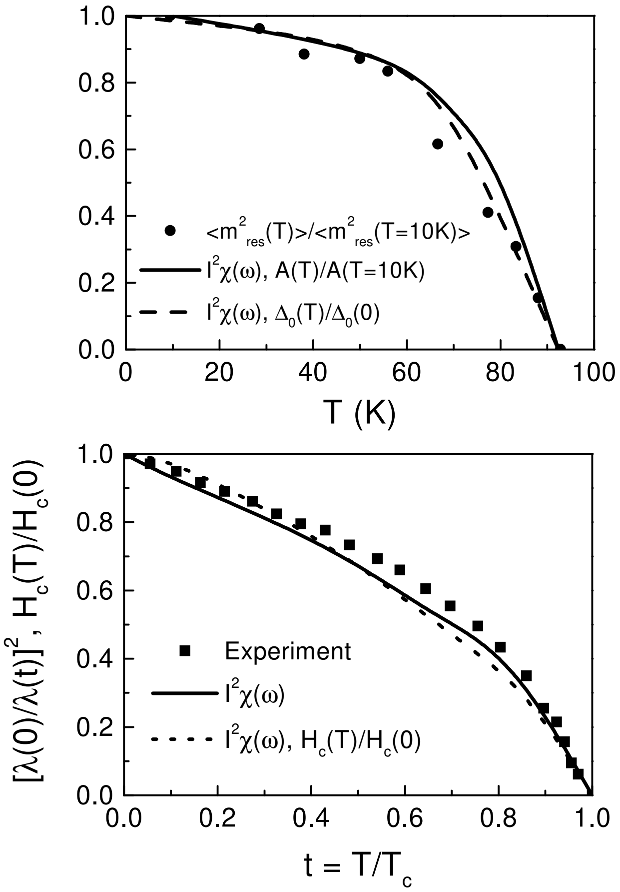

Fig. 19. Top frame: spectral weight under the optical resonance as a function of temperature (solid line) obtained from the optical data of Fig. 6 (top frame, five temperatures only). The solid circles are the data of Dai *et al.* [47] for the normalized area under the spin resonance obtained by neutron scattering. The dashed curve gives our calculated $\Delta_0(T)/\Delta_0(0)$. Bottom frame: the normalized London penetration depth squared $(\lambda(0)/\lambda(T))^2$ *vs.* reduced temperature $t = T/T_c$ (solid line) compared with the experimental results of Bonn *et al.* [4]. The dotted curve gives thermodynamic critical field $H_c(T)/H_c(0)$ *vs.* t.

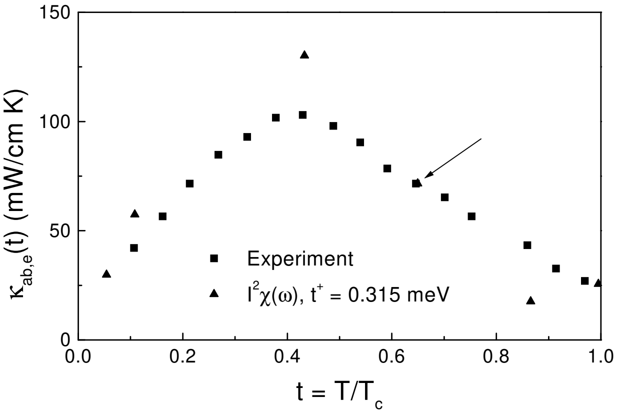

Fig. 20. The electronic part of the thermal conductivity as a function of the reduced temperature $t = T/T_c$. The solid squares are the experimental results of Matsukawa *et al.* [60] and the solid triangles our theoretical result with some impurity scattering included.

	Theory	Experiment	Ref.
$\Delta F(0)$	0.287	0.25	[64,65]
n_s/n	0.33	0.25	[67]
Ω_p	2.36	2.648	[68]
$2\Delta_0/k_BT_c$	5.1	5.0	[66]

Table 1. Some superconducting properties of the twinned YBCO sample: $\Delta F(0)$ is the condensation energy at $T = 0$ in meV/Cu-atom, n_s/n is the superfluid to total carrier density ratio, Ω_p is the plasma frequency in eV.

Other important successes of our Eliashberg calculations are summarized in Table 1. We begin with a discussion of the plasma frequency Ω_p. Referring to Fig. 9 we point out the arrow which shows the frequency at which we made our calculated conductivity agree exactly with experiment. This sets the plasma frequency which is also the total spectral weight under the real part of the conductivity. The optical spectrum sum rule is

$$\int_0^\infty d\omega\, \sigma_1(\omega) = \frac{\Omega_p^2}{8}. \tag{25}$$

A value of $\Omega_p = 2.36\,\mathrm{eV}$ is found which agrees well with the experimental value $2.648\,\mathrm{eV}$ (see Tab. 1). A further comparison of our model with the infrared data is provided by the analysis of the fraction of the total normal-state spectral weight which condenses into the superfluid: n_s/n. Indeed, strong electron-boson coupling reduces the spectral weight of the quasiparticle component of the electronic spectral function $A(\mathbf{k},\omega)$ compared to its non-interacting value by a factor of Z leading at the same time to the appearance of an incoherent component. It is the latter component which is responsible for the Holstein band in the optical conductivity whereas the coherent quasiparticle part gives rise to the Drude term at $T > T_c$ and to the superfluid density at $T = 0$ in the spectra of $\sigma_1(\omega)$ [69]. The values of n_s/n and hence $(Z-1)$ yield an estimate of the strength of renormalization effects in the interacting system. Tanner *et al.* [67] obtained $n_s/n \simeq 0.25$ in crystals of YBCO. This compares well with the value $\simeq 0.33$ which corresponds to $Z \simeq 3$ (at low temperatures) generated in our analysis.

We have also calculated the condensation energy [2] as a function of temperature. Its value at $T = 0$ follows from the normal-state electronic density of states which we take from band structure theory equal to 2.0 states/eV/Cu-atom (double spin) around the middle of the calculated range of values [70]. This gives a condensation energy $\Delta F(0) = 0.287\,\mathrm{meV/Cu}$ — atom which agrees well with the value quoted by Norman *et al.* [64] from the work by Loram *et al.* [65]. (See Tab. 1). This is equivalent to a thermodynamic critical field $\mu_0 H_c(0) = 1.41\,\mathrm{T}$ with $H_c(T)$ defined through $\Delta F(T) = H_c^2(T)/8\pi$. The normalized value $H_c(T)/H_c(0)$ is shown as the dotted line in the bottom frame of Fig. 19 and is seen to follow reasonably, but not exactly, the T dependence of the normalized penetration depth. One further quantity is the ratio of the gap amplitude to the critical temperature which in BCS theory is $2\Delta_0/k_\mathrm{B}T_c = 4.2$ for d-wave. In Eliashberg theory the gap depends on frequency. In this case an unambiguous definition of what is meant by Δ_0 is to use the position in energy of the peak in the quasiparticle density of states which is how the gap Δ_0 is usually defined experimentally for a d-wave superconductor. We get a theoretical value of $2\Delta_0/k_\mathrm{B}T_c \simeq 5.1$ in good agreement with experiment, as shown in Tab. 1.

B. The Compound $\mathrm{Bi_2Sr_2CaCu_2O_{8+\delta}}$

Optical data published by Puchkov *et al.* [46] for optimally doped samples of the compound $\mathrm{Bi_2Sr_2CaCu_2O_{8+\delta}}$ (Bi2212) have first been analyzed by Schachinger and Carbotte [45]. They reported that the normal-state optical scattering rate ($T = 300\,\mathrm{K}$) can be fitted perfectly by an MMP spectrum with $\omega_\mathrm{SF} = 100\,\mathrm{meV}$ and with an high energy cutoff at 400 meV. The inversion of the superconducting state optical scattering rate revealed the coupling of the charge carriers to a resonance found at an energy of 43 meV. This corresponds to the magnetic resonant mode found by Fong *et al.* [71] using inelastic neutron scattering. This mode appears below T_c and its intensity increases with decreasing temperature.

Tu *et al.* [72] recently studied the ab-plane charge dynamics in optimally doped Bi2212 single crystals ($T_c = 91\,\mathrm{K}$) using an experimental technique with much improved signal to noise ratio. They developed an experimentally unambiguous method which examines the maxima and minima of $W(\omega)$, Eq. (8). The authors argued that a comparison of their spectral data with data found for YBCO suggests that a pseudogap exists in Bi2212 above T_c, at least at $T = 100\,\mathrm{K}$. Fig. 21 presents their data (solid lines) together with a theoretical analysis. For $I^2\chi(\omega)$ an MMP spectrum is used and at $T = 295\,\mathrm{K}$ our best fit is found for $\omega_\mathrm{SF} = 82\,\mathrm{meV}$ together with an high energy cutoff 400 meV using theoretical results calculated from Eq. (3) (dotted line). If we calculate the optical scattering rate for the temperatures $T = 200$ and 100 K using the same $I^2\chi(\omega)$ spectrum it becomes obvious that the agreement with experiment deteriorates with decreasing temperature (dotted lines). A comparison of the anomaly in the optical data at $T = 100\,\mathrm{K}$ around 50 meV with the optical data of YBCO (Fig. 8) reveals quite similar behavior which suggests that in Bi2212 a coupling to an optical resonance can actually be seen in the normal state. Indeed, the quality of the data is good enough to allow us to derive $W(\omega)$ by inversion. The result shows a pronounced peak at 43 meV which can be used to modify the $I^2\chi(\omega)$ spectrum. This is shown in Fig. 22. Using this modified spectrum $I^2\chi(\omega)$ to calculate the optical scattering rate for $T = 100\,\mathrm{K}$ results in excellent agreement between experiment and theory (dashed line, Fig. 21 labeled 100 K).

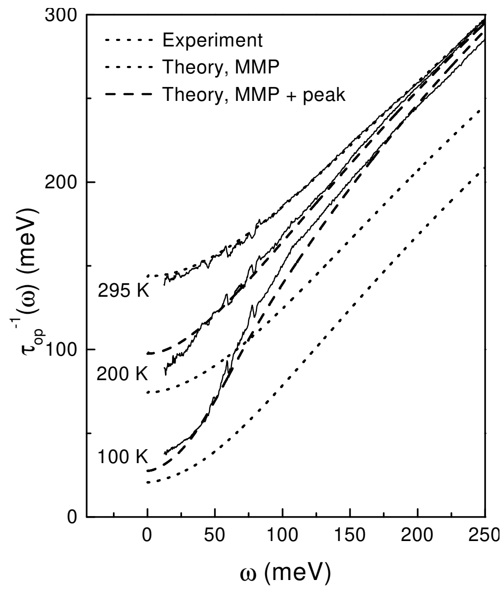

Fig. 21. The temperature dependent ab-plane optical scattering rate for an optimally doped Bi2212 single crystal with $E||a$ in the normal state. The solid lines represent experimental data by Tu *et al.* [72]. The dotted lines give the theoretical result calculated using Eq. (3) and a $I^2\chi(\omega)$ which is just an MMP spectrum with $\omega_{\rm SF} = 82$ meV. At $T = 295$ K theory reproduces experiment almost ideally; this agreement deteriorates at lower temperatures. Finally, the dashed lines present theoretical results found for the same MMP spectrum as before but now with coupling to the 43 meV optical resonance added.

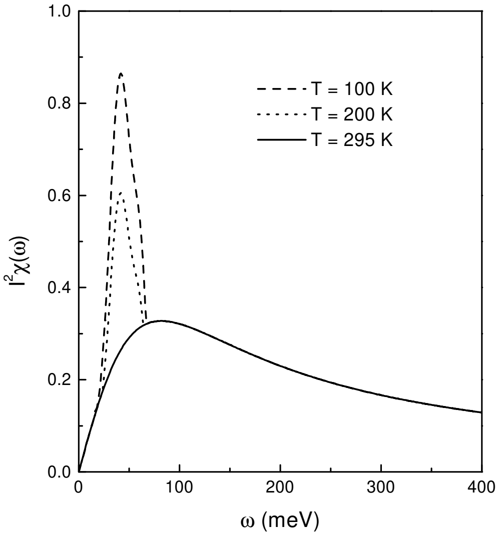

Fig. 22. The charge carrier-spin excitation spectral density $I^2\chi(\omega)$ determined from normal-state optical scattering data shown in Fig. 21 for optimally doped Bi2212 single crystals. The solid curve is for $T = 295$ K, the dotted curve for 200 K, and the dashed one for 100 K. Note the growth in strength of the 43 meV optical resonance as the temperature is lowered.

The $T = 200$ K data show a similar, but less pronounced, anomaly. It is not possible to derive a $W(\omega)$ directly from the data so we simply use the $I^2\chi(\omega)$ found for 100 K and reduce the size of the 43 meV peak until best agreement between experiment and theory is reached (dashed line in Fig. 21 labeled 200 K). This results in an $I^2\chi(\omega)$ presented in Fig. 22 which still contains a pronounced contribution from the coupling of the charge carriers to the optical resonance (dotted line). From this we can conclude that the optical resonance, and probably connected with it, the magnetic resonant mode exists at least up to 200 K. Nevertheless, our result for 295 K indicates that at this temperature the optical resonance no longer exists.

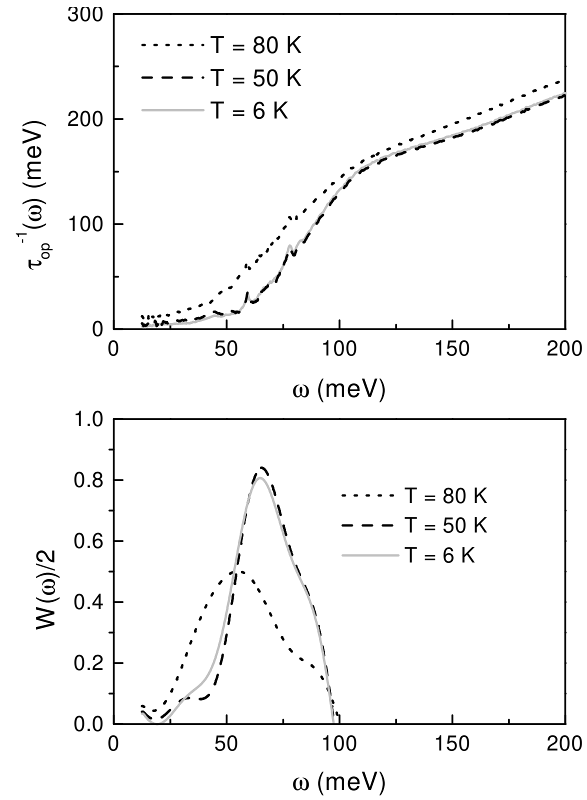

Fig. 23. Top frame: optical scattering rate $\tau_{\rm op}^{-1}(T,\omega)$ in meV for optimally doped, untwinned Bi2212 single crystals [72]. Bottom frame: function $W(\omega)/2$ *vs.* ω in the region of the optical resonance.

We will now concentrate on the superconducting state and study the temperature dependence of $I^2\chi(\omega)$ below T_c. The top frame of Fig. 23 presents the infrared scattering rate as measured by Tu *et al.* [72] for three temperatures, namely 6 K (gray solid line), 50 K (dashed line), and 80 K (dotted line). In comparison with similar results for YBCO (top frame of Fig. 6) we recognize that even at 80 K Bi2212 shows a very strong suppression of $\tau_{\rm op}^{-1}(\omega)$ at energies below 50 meV which is an indication of stronger coupling of the charge carriers to the optical resonance. The bottom frame of this figure shows the function $W(\omega)/2$ derived from experiment with the high energy negative parts suppressed because we want to concentrate on the optical resonance. It increases as T is lowered and shows only little further variation below 50 K. In $W(\omega)/2$ the resonance peak is positioned at the resonance energy E_r plus the gap value $\Delta_0(T)$ and with the temperature dependence of the gap accounted for, we can conclude that the position of the resonance is temperature independent and stays at $E_r = 43$ meV, the energy at which the magnetic resonant mode is found by inelastic neutron scattering [71]. The coupling of the charge carriers to a boson at 43 meV has also been observed in photoemission [73] and tunneling [74] work on Bi2212 and the 43 meV magnetic resonant mode seems to be the obvious candidate for the origin of this boson.

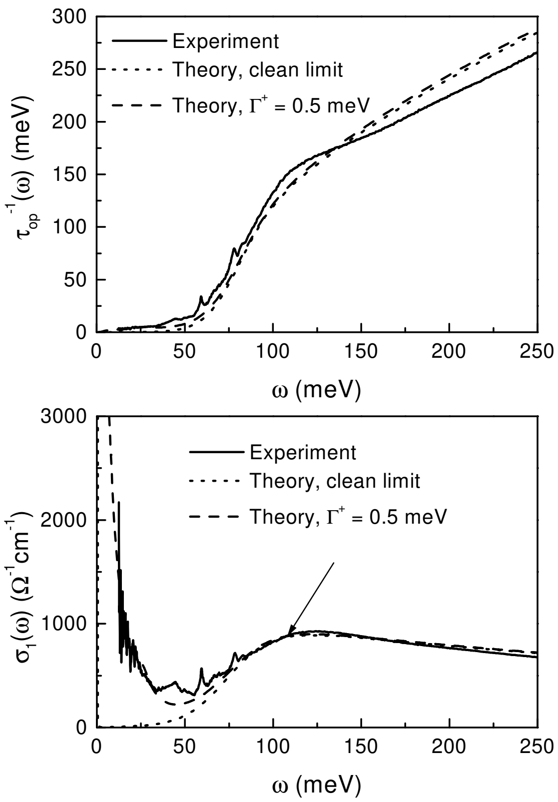

Fig. 24. The top frame gives the optical scattering rate $\tau_{\rm op}^{-1}(\omega)$ *vs.* ω for optimally doped Bi2212 single crystals at a temperature of 6 K. The experimental results give the solid curve and our clean limit theoretical fit to it is the dotted curve. The dashed curve presents theoretical results for a system with impurity scattering in the unitary limit described by the parameter $\Gamma^+ = 0.5$ meV and $c = 0$. The lower frame gives a comparison of the real part of the in-plane optical conductivity $\sigma_1(\omega)$ vs. ω for the two models already presented in the top frame. The solid curve is the experimental data, the dotted curve the clean limit theoretical result, and the dashed curve the theoretical result for the system with impurities.

Fig. 24 demonstrates the agreement which can be achieved between theory and experiment. The top frame shows the infrared scattering rate $\tau_{\rm op}^{-1}(\omega)$ *vs.* ω for $T = 6$ K. The solid line gives the experimental data while the dashed and dotted curves represent theoretical results for a clean limit system and for a system with impurity scattering in the unitary limit ($\Gamma^+ = 0.5$ meV) respectively. The differences in the scattering rate are marginal for these two model systems, nevertheless, they become important when the real part of the optical conductivity $\sigma_1(\omega)$ is investigated. The bottom frame of Fig. 24 shows the results. The solid line is experiment, the dotted line is theory for the clean limit system. It reproduces nicely the maximum in $\sigma_1(\omega)$ around 120 meV and the high energy tail. At energies below 75 meV the clean limit results deviates strongly from experiment towards nearly zero values and show a very pronounced, narrow peak around $\omega = 0$. Results for the system with impurities treated in the unitary limit ($\Gamma^+ = 0.5$ meV, dashed line) display all important features observed in the experimental data. We see, as in the case of YBCO, that impurities affect only the low energy region ($\omega < 60$ meV), the region $60 \le \omega \le 100$ meV is dominated by the coupling to the optical resonance modeled in the $I^2\chi(\omega)$ while the energy region $\omega > 120$ meV is determined by the normal-state MMP part of $I^2\chi(\omega)$ as has already been described for the YBCO compound.

The bottom frame of Fig. 24 contains an arrow which points out the frequency at which we made our calculated $\sigma_1(\omega)$ to agree exactly with experiment. (This was only done for the clean limit calculation, the same scaling was used for the system with impurities.) This sets the plasma frequency $\Omega_p = 2.3$ eV which is to be compared with the $\Omega_p = 1.98$ eV used by Tu *et al.* [72]. Finally, we found for the superconducting gap at $T = 6$ K a value of 25 meV. This is certainly smaller than the value of 34 meV reported by Rübhausen *et al.* [75] from Raman spectroscopy on Bi2212 single crystals with a T_c of 95 K.

C. Application to Other Cuprates

In contrast to the systems studied so far $Tl_2Ba_2CuO_{6+\delta}$ (Tl2201) is a monolayer compound while YBCO, Bi2212 and $YBa_2Cu_4O_8$ (Y124) are bilayer compounds. Moreover, Tl2201 is the only system with tetragonal symmetry, all the other compounds are of orthorhombic symmetry. Its $T_c \sim 90$ K and this is similar to the T_c of YBCO and Bi2212. Y124, on the other hand has a slightly lower T_c of 82 K and shows properties which resemble a moderately underdoped YBCO compound.

In Fig. 25 we show our result for the normal-state $\tau_{\rm op}^{-1}(\omega)$ [46] related to the conductivity by Eq. (7) for Tl2201 with $T_c = 90$ K at temperature $T = 300$ K. The solid curve is the data of Puchkov *et al.* [46]. The dotted curve is our best fit for $\omega_{\rm SF} = 30$ meV with I^2 adjusted to get the correct absolute value of the scattering rate at $T = 300$ K and $\omega = 200$ meV. We see that this value of $\omega_{\rm SF}$ does not give a satisfactory fit to the data. The dash-dotted curve, however, fits the data well and corresponds to $\omega_{\rm SF} = 100$ meV. This fit provides us with a model $I^2\chi(\omega)$ valid for the normal state of Tl2201. This $I^2\chi(\omega)$ is then used to calculate the anisotropy parameter g from the solution of the linearized imaginary axis Eliashberg equations (10) for the critical temperature $T_c = 90$ K. As a result of this procedure all necessary parameters are fixed and we can now proceed to study the superconducting state.

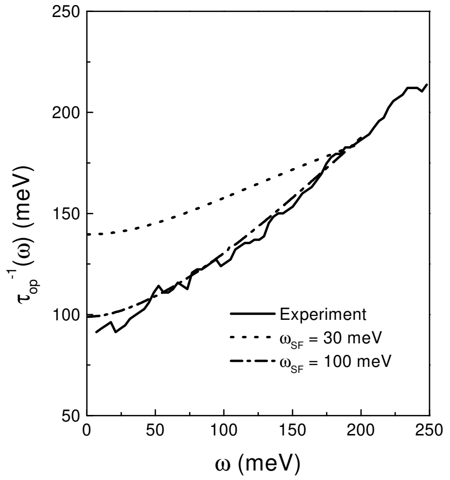

Fig. 25. The normal-state optical scattering rate $\tau_{\mathrm{op}}^{-1}(\omega)$ *vs.* ω for Tl2201 with a $T_c = 90\,\mathrm{K}$ obtained from the work of Puchkov *et al.* [46] (solid curve). The dash-dotted curve from theory based on Eq. (3) with an MMP model spectral density using a spin fluctuation frequency $\omega_{\mathrm{SF}} = 100\,\mathrm{meV}$ gives good agreement while the choice of 30 meV (dotted curve) does not.

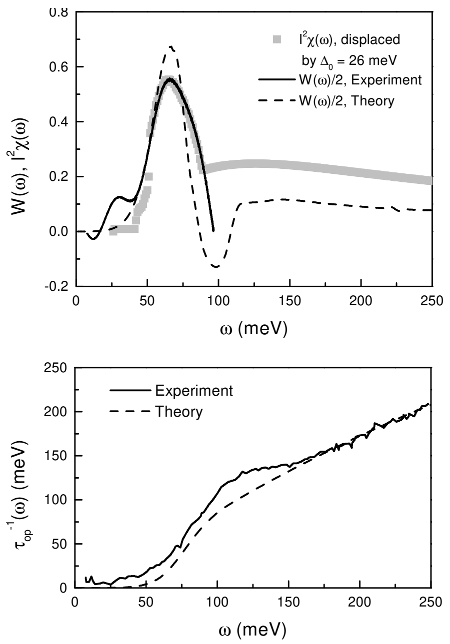

Fig. 26. The top frame gives our model for the spin-fluctuation spectral density (displaced by the theoretical gap $\Delta_0 = 26\,\mathrm{meV}$) for Tl2201 in the superconducting state at $T = 10\,\mathrm{K}$ (gray solid squares). The dashed line is $W(\omega)$ obtained from the calculated conductivity and the black solid line is the coupling to the resonance found directly from experiment. (The high frequency part has been omitted.) It was used in constructing the model $I^2\chi(\omega)$. The bottom frame shows the optical scattering rate at $T = 10\,\mathrm{K}$ (solid line) and the theoretical fit to experiment found from Eliashberg theory.

Results are shown in Fig. 26. The solid line in the top frame shows the optical resonance obtained from inversion of the experimental superconducting optical scattering rate, presented in the bottom frame of this figure (solid line). The gray squares are the $I^2\chi(\omega)$ used in the calculations displaced in energy by the gap $\Delta_0 = 26\,\mathrm{meV}$. It is constructed completely from experiment and we followed the procedure already described in detail for the YBCO compound. The dashed curve, finally, is the result of an inversion of theoretical data, shown in the bottom frame of this figure (dashed line) and we see that it agrees reasonably well with experiment (solid line). These results allowed Schachinger and Carbotte [44] to predict for Tl2201 a spin resonance at 43 meV. They also predicted that the resonance should be less pronounced and broader in Tl2201 than in YBCO or Bi2212. Recently He *et al.* [76] succeeded in preparing a Tl2201 sample big enough for inelastic magnetic neutron scattering. This sample consists of about 300 coaligned optimally doped Tl2201 single crystals. This experiment confirmed the existence of a magnetic resonant mode in Tl2201 below T_c which is located at about 47 meV and which appears to be narrower than the resonances observed in YBCO or Bi2212. This is in slight disagreement with the results of Schachinger and Carbotte [44] and this disagreement could probably be explained by the poorer quality of the samples used by Puchkov *et al.* [46] for the optical measurements many years ago. Other optical data are not available. Nevertheless, the basic agreement between the observation of Schachinger and Carbotte [44] that the charge carriers in Tl2201 couple to an optical resonance and the subsequent observation of a magnetic resonant mode at about the same energy by He *et al.* [76] using inelastic neutron scattering is quite important. It proves that magnetic resonant modes are not restricted to bilayer compounds and that we seem to be confronted with a unified phenomenological picture.

The optical resonance peak is not observed in all systems as is illustrated in Fig. 27 for an overdoped sample of Tl2201 with $T_c = 23\,\mathrm{K}$. In this case a fit to the $T = 300\,\mathrm{K}$ normal-state data (solid gray curve) with an MMP model gives $\omega_{\mathrm{SF}} = 100\,\mathrm{meV}$ (gray dashed curve). The same spectrum also produces a good fit (black dashed line) to the data at $T = 10\,\mathrm{K}$ (black solid line) in the superconducting state. There is no need to introduce a spin resonance. Indeed the black solid curve for the measured optical scattering rate $\tau_{\mathrm{op}}^{-1}(\omega)$ is smooth and increases gradually as ω increases with no clear sharp rise at any definite frequency in sharp contrast with Fig. 26. We conclude from this analysis that the resonance observed in some cuprates with high values of T_c at optimum doping is not present in all cases and in particular there is no evidence for such a resonance in overdoped Tl2201 with $T_c = 23\,\mathrm{K}$. In this case a standard MMP spectrum of the form (24) gives an adequate representation of the superconducting state optical scattering rate as a function of ω with the same spectral density as was determined by the data at $T = 300\,\mathrm{K}$. This is in contrast to the other cases studied above for which the onset of superconductivity appears to produce essential modifications of the underlying spectral density $I^2\chi(\omega)$.

We extend our analysis to the material Y124 ($T_c =$

82 K) where we predict from Fig. 28 (top frame, solid curve) a resonance at 38 meV. (This is below the energy of 41 meV for the resonance in YBCO which is not surprising as it is a well established property of bilayer high-T_c cuprates that the energy of the magnetic resonant mode tracks T_c in underdoped systems [47] and the optical resonance seems to be closely related to this magnetic resonant mode.) The top frame of this figure demonstrates the agreement with $W(\omega)/2$ and $I^2\chi(\omega)$ which was shifted by the theoretical gap $\Delta_0 = 24$ meV which is a prediction of our calculations as, to our knowledge, no experimental data exist for this material. The bottom frame of Fig. 28 presents our comparison between experimental and theoretical optical scattering rates. The normal-state scattering rate (gray lines) at $T = 300$ K gives evidence for the existence of a high energy background as the experimental data (gray solid line) are best fit by an MMP spin-fluctuation spectrum as described by Eq. (24) with $\omega_{\mathrm{SF}} = 80$ meV and a high energy cutoff of 400 meV (gray dashed line). The black lines compare the theoretical results (dashed line) with experiment [46] (solid line) in the superconducting state at $T = 10$ K. The signature of the optical resonance, the sharp rise in $\tau_{\mathrm{op}}^{-1}(\omega)$ starting at around 50 meV is correctly reproduced by theory. For $\omega > 120$ meV the experimental scattering rate shows only a weak energy dependence and the theoretical prediction starts to deviate from experiment. This is in contrast to our results found for all other compounds and could be related to the fact that the Y124 compound shows features of an underdoped system.

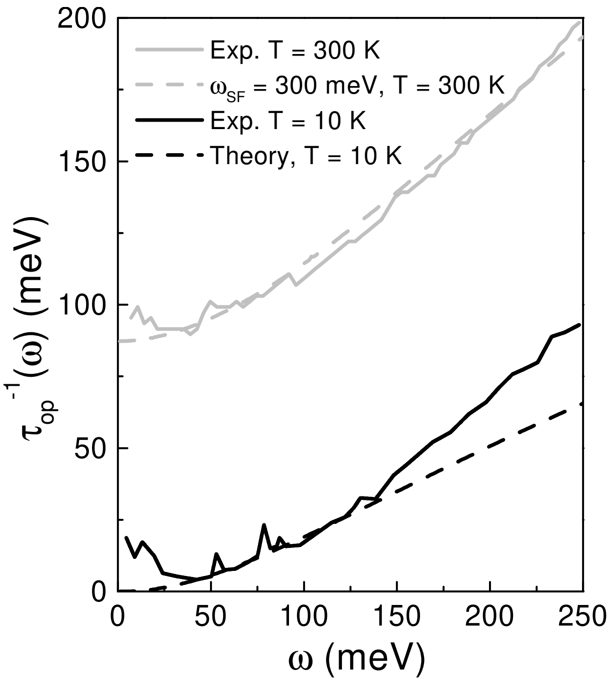

Fig. 27. The optical scattering rates in an overdoped sample of Tl2201 with a $T_c = 23$ K. The solid lines represent experimental data and the dashed lines fits. The gray curves apply in the normal-state at $T = 300$ K and the black curves in the superconducting state at $T = 10$ K. No optical resonance peak is found in this case.

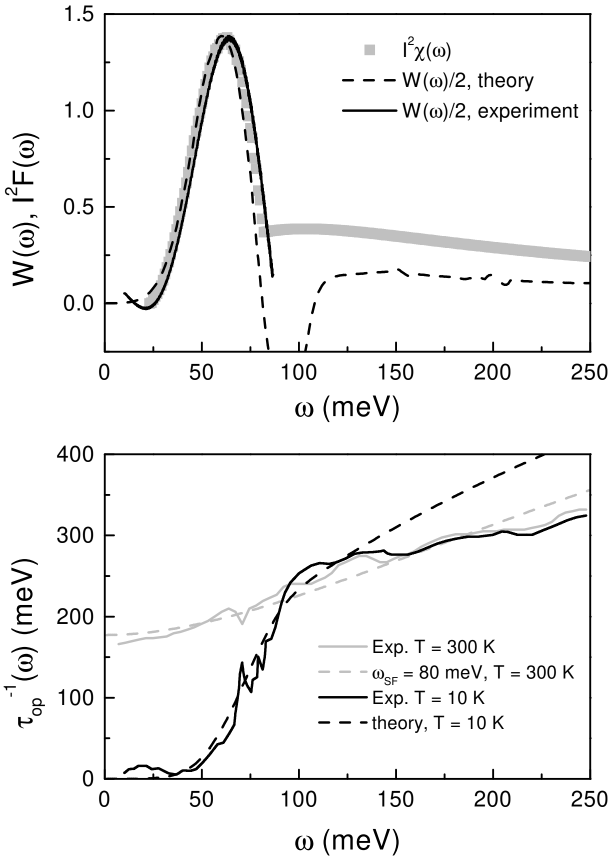

Fig. 28. The same as Fig. 26 but for the material Y124. The spin-fluctuation spectral density $I^2\chi(\omega)$ was displaced by the theoretical gap $\Delta_0 = 24$ meV in the top frame. In addition, the grayed lines in the bottom frame of this figure show the comparison between experimental and theoretical normal-state data at $T = 300$ K. Due to this comparison $\omega_{\mathrm{SF}} = 80$ meV for the MMP spectrum of Eq. (24).

IV. SUMMARY

An extended Eliashberg theory can be applied to describe the superconducting properties of hole doped high-T_c cuprates. The extension goes in two directions: first, it is essential to allow the pairing potential to have $d_{x^2-y^2}$ symmetry, and, second, the charge carrier — exchange boson interaction leading to pairing has to be modeled using a phenomenological approach because the microscopic origin of the attractive interaction between the charge carriers is still unknown.

An anomalous steep rise in the superconducting state optical scattering rate observed in optimally doped YBCO in the energy range $50 \leq \omega \leq 90$ meV was attributed to the coupling of the charge carriers to an optical resonance located at about 41 meV. This optical resonance has its counterpart in a magnetic resonant mode which can be observed in YBCO at the same energy by inelastic neutron scattering. This resonance is not observed above T_c in the normal-state and the normal-state infrared scattering rate too does not develop any anomaly. Further experimental data on the temperature dependence of the infrared scattering rate and of the magnetic resonance proved further agreement as the area under the optical resonance is seen to have the same temperature dependence as the 41 meV magnetic resonant mode. All this resulted in a definite procedure which allows a phenomenological charge carrier — exchange boson interaction spectral density $I^2\chi(\omega)$ to be derived which reflects the coupling of the charge carriers to the optical resonance and also describes properly the almost linear frequency dependence of the normal-state infrared scattering rate. Using this phenomenological $I^2\chi(\omega)$ as the kernel of an extended Eliashberg theory allows us not only to reproduce the experimental infrared optical data, it also allows to reproduce properly the temperature dependence of the microwave conductivity, of the London penetration depth, and of numerous other superconducting properties.

This success justifies the extension of this analysis to other compounds, like Bi2212, Tl2201, and Y124 for which less extensive experimental data are available. The latest high quality optical data on Bi2212 proved that, also in this case, the coupling of the charge carriers to an optical resonance at 43 meV can be associated with an anomalous steep rise in the superconducting state infrared scattering rate. In contrast to YBCO the anomaly in the infrared optical scattering rate can also be observed in the normal state. This optical resonance has, in the superconducting state, its counterpart in a magnetic resonant mode observed by inelastic neutron scattering at 43 meV. This mode has, so far, not been observed in the normal state of optimally doped Bi2212. The method to derive a phenomenological $I^2\chi(\omega)$ from optical data developed for YBCO can also be applied to the compound Bi2212 and leads, again, to a temperature dependent kernel $I^2\chi(\omega)$ and the extended Eliashberg theory allows an excellent reproduction of some superconducting state properties.

A similar anomaly can be observed in the superconducting state low-temperature infrared scattering rate of Tl2201 and Y124. It has, consequently, been interpreted as the coupling of charge carriers to an optical resonance, not present above T_c. Recently, in the monolayer compound Tl2201 a magnetic resonant mode has been observed in the superconducting state but at a slightly higher energy than predicted from optical data. Nevertheless, this fact is quite important because it established that the existence of a magnetic resonant mode is not restricted to bilayer compounds. The existence of a magnetic resonant mode is still to be proved in Y124, in which an optical resonance seems to exist at an energy of 38 meV. For both compounds, an extended Eliashberg theory together with a phenomenologically derived kernel $I^2\chi(\omega)$ resulted in a good reproduction of the optical data. Not enough information about a possible temperature dependence of the $I^2\chi(\omega)$ in these compounds is available to extend the theoretical analysis to other superconducting state properties.

All this established a unified phenomenological picture for hole doped high-T_c cuprates which interpretes anomalies in the charge carrier dynamics observed in optimally and overdoped samples as a signature of spin degrees of freedom in these compounds.

ACKNOWLEDGMENTS

This research was supported by the Natural Sciences and Engineering Research Council of Canada (NSERC) and by the Canadian Institute for Advanced Research (CIAR). The authors thank Drs. D. N. Basov, C. C. Homes, and J. J. Tu for discussions and for making their data available to us.

[1] G. M. Eliashberg, Zh. Eksp. Teor. Fiz. **38**, 966 (1960); Sov. Phys. JETP **11**, 696 (1960).
[2] J. P. Carbotte, Rev. Mod. Phys. **62**, 1027 (1990) gives an excellent review.
[3] W. N. Hardy, D. A. Bonn, D. C. Morgan, R. Liang, K. Zhang, Phys. Rev. Lett. **70**, 3999 (1993).
[4] D. A. Bonn, S. Kamal, K. Zhang, R. Liang, D. J. Baar, E. Klein, W. N. Hardy, Phys. Rev. B **50**, 4051 (1994).
[5] Z. X. Shen, D. S. Dessau, B. O. Wells, D. M. King, W. E. Spicer, A. J. Arko, D. Marshall, L. W. Lombardo, A. Kapitulik, P. Dickinson, S. Doniach, J. DiCarlo, A. G. Loeser, C. H. Park, Phys. Rev. Lett. **70**, 1553 (1993).
[6] D. H. Wollmann, D. J. Van Harlington, W. C. Lee, D. M. Ginsberg, A. J. Legget, Phys. Rev. Lett. **71**, 2134 (1993).
[7] C. C. Tsuei, J. R. Kirtley, C. C. Chi, L. S. Yu-Jahnes, A. Gupta, T. Shaw, J. Z. Sun, M. B. Ketchen, Phys. Rev. Lett. **73**, 539 (1994).
[8] D. M. Broun, D. C. Morgan, R. J. Ormeno, S. F. Lee, A. W. Tyler, A. P. Mackenzie, J. R. Waldram, Phys. Rev. B **56**, R11 443 (1997).
[9] F. Marsiglio, J. P. Carbotte, in *Handbook on Superconductivity: Conventional and Unconventional, Vol. 1*, edited by K. H. Bennemann, J. B. Ketterson (Springer, Berlin, 2003), p. 233.
[10] W. L. McMillanm, J. M. Rowell, in *Superconductivity*, edited by R. D. Parks (Marcel Dekker Inc., New York, 1969), p. 561.
[11] B. R. Joyce, P. L. Richards, Phys. Rev. Lett. **24**, 1007 (1970).
[12] P. B. Allen, Phys. Rev. B **3**, 305 (1971).
[13] B. Farnworth, T. Timusk, Phys. Rev. B **10**, 2799 (1974); *ibid.* **14**, 5119 (1976).
[14] E. Schachinger, J. P. Carbotte, F. Marsiglio, Phys. Rev. B **56**, 2738 (1997).
[15] E. Schachinger, J. P. Carbotte, Phys. Rev. B **57**, 13337 (1998).

[16] E. Schachinger, J. P. Carbotte, Phys. Rev. B **57**, 7970 (1998).
[17] E. Schachinger, I. Schürrer, Condens. Matter. Phys. **1**, 69 (1998).
[18] A. Millis, H. Monien, D. Pines, Phys. Rev. B **46**, 14803 (1990).
[19] P. Monthoux, D. Pines, Phys. Rev. B **47**, 6069 (1993); Phys. Rev. B **49**, 4261 (1994); Phys. Rev. B **50**, 16015 (1994).
[20] D. A. Bonn, P. Dosanjh, R. Liang, W. H. Hardy, J. Phys. Chem. Solids **56**, 1941 (1995).
[21] H. Srikanth, B. A. Willemsen, T. Jacobs, S. Sridhar, A. Erb, R. Flükinger, Phys. Rev. B **55**, R14733 (1997).
[22] M. Matsukawa, T. Mizukoshi, K. Noto, Y. Shiohara, Phys. Rev. B **53**, R6043 (1996).
[23] C. M. Varma, P. B. Littlewood, S. Schmitt-Rink, E. Abrahams, A. E. Ruckenstein, Phys. Rev. Lett. **63**, 1936 (1989); **64**, 497(E) (1990).
[24] F. Marsiglio, T. Startseva, J. P. Carbotte, Phys. Lett. A **245**, 172 (1998).
[25] J. P. Carbotte, E. Schachinger, D. N. Basov, Nature (London) **401**, 354 (1999).
[26] D. Munzar, C. Bernhard, M. Cardona, Physica C **318**, 547 (1999).
[27] F. Marsiglio, J. P. Carbotte, Aust. J. Phys. **50**, 975 (1997); Aust. J. Phys. **50**, 1011 (1997).
[28] W. Lee, D. Rainer, W. Zimmermann, Physica C **159**, 535 (1984).
[29] O. V. Dolgov, E. G. Maksimov, S. V. Shulga, in *Electron-Phonon Interaction in Oxide Superconductors*, edited by R. Baquero (World Scientific, Singapore, 1991), p. 30.
[30] S. V. Shulga, O. V. Dolgov, E. G. Maksimov, Physica C **178**, 266 (1991).
[31] I. Schürrer, E. Schachinger, J. P. Carbotte, Physica C **303**, 287 (1998).
[32] Y. Nambu, Phys. Rev. **117**, 648 (1960).
[33] F. Marsiglio, J. Supercond. **12**, 163 (1999).
[34] C. Jiang, E. Schachinger, J. P. Carbotte, D. N. Basov, T. Timusk, Phys. Rev. B **54**, 1264 (1996).
[35] E.H. Kim, Phys. Rev. B **58**, 2452 (1997).
[36] R. J. Radtke, V. N. Kostur, K. Levin, Phys. Rev. B **53**, R522 (1996).
[37] K.G. Sandeman, A.J. Schofield, Phys. Rev. B **63**, 094510 (2001).
[38] T. Xiang, J. M. Wheatley, Phys. Rev. Lett. **76**, 4632 (1996).
[39] O. K. Anderson, O. Jepsen, A. Lichtenstein, I. I. Mazin, Phys. Rev. B **49**, 4145 (1994).
[40] T. Xiang, C. Panagopoulos, and J.R. Cooper, Intern. J. Mod. Phys. B **12**, 1007 (1998).
[41] P. J. Hirschfeld, S. M. Quinlan, D. J. Scalapino, Phys. Rev. B **55**, 12742 (1997).
[42] D. N. Basov, R. Liang, B. Dabrovski, D. A. Bonn, W. N. Hardy, T. Timusk, Phys. Rev. Lett. **77**, 4090 (1996).
[43] Ph. Bourges, Y. Sidis, H. F. Fong, B. Keimer, L. P. Regnault, J. Bossy, A. S. Ivanov, D. L. Lilius, I. A. Aksay, in *High Temperature Superconductivity*, edited by S. E. Barnes, *et al.*, CP483 (American Institute of Physics, Amsterdam, 1999), p. 207.
[44] E. Schachinger, J. P. Carbotte, Phys. Rev. B **62**, 9054 (2000).
[45] E. Schachinger, J. P. Carbotte, Physica C **341–348**, 79 (2000).
[46] A. V. Puchkov, D. N. Basov, T. Timusk, J. Phys.: Cond. Matt. **8**, 10049 (1996).
[47] P. Dai, H. A. Mook, S. M. Hayden, G. Aeppli, T. G. Perring, R. D. Hunt, F. Doğan, Science **284**, 1344 (1999).
[48] C. C. Homes, T. Timusk, R. Liang, D. A. Bonn, W. N. Hardy, Phys. Rev. Lett. **71**, 1645 (1993).
[49] E. Schachinger, J. P. Carbotte, D. N. Basov, Europhys. Lett. **54**, 380 (2001).
[50] E. Schachinger, J. P. Carbotte, Physica C **364–365**, 13 (2001).
[51] Ar. Abanov, A. V. Chubukov, J. Schmalian, Phys. Rev. B **63**, 180510(R) (2001).
[52] T. Dahm, D. Manske, L. Tewordt, Phys. Rev. B **60**, 14 888 (1999).
[53] E. Abrahams, C.M. Varma, Proc. Nat. Acad. Sci. **97**, 5714, (2000).
[54] T. Valla, A. V. Fedorov, P. D. Johnson, B. D. Wells, S. L. Hulbert, G. Li, G. D. Ju, N. Koshizuka, Science **285**, 2110 (1999).
[55] A. Kamenski, A. J. Mesot, H. Fretwell, J. C. Campuzano, M. R. Norman, M. Randerias, H. Ding, T. Sato, T. Takahashi, T. Mochidu, K. Kadowaki, H. Hoechst, Phys. Rev. Lett. **84**, 1788 (2000).
[56] S. Hensen, G. Müller, C. T. Rieck, K. Scharnberg, Phys. Rev. B **56**, 6237 (1997).
[57] A. H. Hosseini, R. Harris, S. Kamal, P. Dosanjh, J. Preston, R. Liang, W. N. Hardy, D. A. Bonn, Phys. Rev. B **60**, 1349 (1999).
[58] E. Schachinger, J. P. Carbotte, Phys. Rev. B **64**, 094501 (2001).
[59] A. Hosseini, S. Kamal, D. A. Bonn, R. Liang, W. N. Hardy, Phys. Rev. Lett. **91**, 1298 (1998).
[60] M. Matsukawa, T. Mizukoshi, K. Noto, Y. Shiohara, Phys. Rev. B **53**, R6043 (1996).
[61] M. C. Nuss, P. M. Mankiewich, N. L. O'Malley, E. H. Westwick, Phys. Rev. Lett. **66**, 3305 (1991).
[62] E. J. Nicol, J. P. Carbotte, Phys. Rev. B **44**, R7741 (1991).
[63] D. A. Bonn, R. Liang, T. M. Risemann, D. J. Baar, D. C. Morgan, K. Zhang, P. Dosanjh, T. L. Duty, A. MacFarlane, G. D. Morris, J. H. Brewer, W. H. Hardy, C. Kallin, A. J. Berlinsky, Phys. Rev. B **47**, 11314 (1993).
[64] M. R. Norman, M. Randeira, B. Janko, J. C. Campuzano, Phys. Rev. B **61**, 14742 (2000).
[65] J. W. Loram, K. A. Mirza, P. F. Freeman, Physica C **171**, 243 (1990).
[66] M. Gurvitch, J. M. Valles Jr., A. M. Cucolo, R. C. Dynes, J. P. Garno, L. F. Schneemeyer, J. V. Waszak, Phys. Rev. Lett. **63**, 1008 (1989).
[67] D. B. Tanner, H. L. Liu, M. A. Quijada, A. M. Zibold, H. Berger, R. J. Kelley, M. Onellion, F. C. Chou, D. C. Johnston, J. P. Rice, D. M. Ginsberg, J. T. Markert, Physica B **244**, 1 (1998).
[68] C. C. Homes, D. A. Bonn, R. Liang, W. N. Hardy, D. N. Basov, T. Timusk, B. P. Claymann, Phys. Rev. B **60**, 9782 (1999).
[69] In BCS theory, the Drude contribution completely condenses at $T = 0$ only in the clean limit. The clean limit is well-justified in view of large values of the electronic mean free path extracted from the microwave data by A. Hosseini, R. Harris, S. Kamal, P. Dosanjh, J. Preston, R. Liang, W. N. Hardy, D. A. Bonn, Phys. Rev. B

60, 1349 (1999).
[70] A. Junod, *Physical Properties of High T_c Superconductors II*, edited by D. M. Ginsberg (World Scientific, Singapore, 1990), p. 43.
[71] H. F. Fong, P. Bourges, L. P. Regnault, A. Ivanov, G. D. Gu, N. Koshizuka, B. Keimer, Nature (London) **398**, 588 (1999).
[72] J. J. Tu, C. C. Homes, G. D. Gu, D. N. Basov, S. M. Loureiro, R. J. Cava, M. Strongin, Phys. Rev. B **66**, 144514 (2002).
[73] P. D. Johnson, T. Valla, A. V. Fedorov, Z. Yusof, B. O. Wells, Q. Li, A. R. Moodenbaugh, G. D. Gu, N. Koshizuka, C. Kendziora, Sha Jian, D. G. Hinks, Phys. Rev. Lett. **87**, 177007 (2001).
[74] J. F. Zasadzinski, L. Ozyuzer, N. Miyakawa, K. E. Gray, D. G. Hinks, C. Kendziora, Phys. Rev. B **87**, 067005 (2001).
[75] M. Rübhausen, P. Guptasarma, D. G. Hinks, M. V. Klein, Phys. Rev. B **58**, 3462 (1998).
[76] H. He, P. Bourges, Y. Sidis, C. Ulrich, L. P. Regnault, S. Pailhès, N. S. Berzigiarova, N. N. Kolesnikov, B. Keimer, Science **295**, 1045 (2002).

ЗАСТОСУВАННЯ РОЗШИРЕНОЇ ТЕОРІЇ ЕЛІАШБЕРҐА ДО ВИСОКОТЕМПЕРАТУРНИХ КУПРАТІВ

Е. Шахінґер[1], Дж. Карботт[2]
[1]*Інститут теоретичної фізики, Технічний університет Ґрацу, A–8010, Ґрац, Австрія*
[2]*Кафедра фізики й астрономії, Університет МакМастер, Гамільтон, Онтаріо, Канада, L8S 4M1*

Останнім часом з'явилася єдина феноменологічна картина леґованих дірками високотемпературних купратів для спінової та зарядкової спектроскопії. Спектральні аномалії інтерпретують як доказ з'єднання носія заряду з наявним в оптичній провідності колективним спіновим збудженням у кутово-розділеній фотоемісії та в даних тунелювання. Цими аномаліями можна скористатися для виявлення наближеної картини спектральної густини взаємодії між носієм заряду й обмінним бозоном $I^2\chi(\omega)$, яку пізніше можна використати в розширеному формалізмі Еліашберґа для аналізу нормальних та надпровідних властивостей оптимально леґованих та надлеґованих купратів. У статті зосереджно увагу на сучасному стані проблеми, а також показано іноді вражаючу узгодженість між експериментальними даними та теоретичним передбаченням.